Technical Memorandum ERL WPL-191

OPTICAL REMOTE SENSING

Lilybeth Mosquera Kovacs
James H. Churnside

Wave Propagation Laboratory
Boulder, Colorado
February 1991

noaa NATIONAL OCEANIC AND ATMOSPHERIC ADMINISTRATION / Environmental Research Laboratories

NOAA Technical Memorandum ERL WPL-191

OPTICAL REMOTE SENSING

Lilybeth Mosquera Kovacs
Cooperative Institute for Research in Environmental Sciences
University of Colorado
Boulder, Colorado

James H. Churnside

Wave Propagation Laboratory
Boulder, Colorado
February 1991

UNITED STATES DEPARTMENT OF COMMERCE

Robert A. Mosbacher
Secretary

NATIONAL OCEANIC AND ATMOSPHERIC ADMINISTRATION

John A. Knauss
Under Secretary for Oceans and Atmosphere/Administrator

Environmental Research Laboratories

Joseph O. Fletcher
Director

NOTICE

Mention of a commercial company or product does not constitute an endorsement by NOAA/ERL. Use of information from this publication concerning proprietary products or the tests of such products for publicity or advertising purposes is not authorized.

For sale by the National Technical Information Service, 5285 Port Royal Road
Springfield, VA 22161

TABLE OF CONTENTS

OPTICAL REMOTE SENSING

Lilybeth Mosquera Kovacs[1]
James H. Churnside[2]

ABSTRACT. The random absorption and refraction experienced by the electromagnetic wave produce fluctuations in the wave amplitude and phase as observed at a remote point. The impact of these fluctuations on a double-spatial filtering receiver is evaluated by performing a diffraction analysis on the system. The diffraction analysis covers a complete study of an electromagnetic wave propagating through the atmosphere, and through the double-spatial filtering receiver in order to obtain the wave field at the focal plane. The transmitter can be any natural or artificial source. The choice in this configuration is the sun. Theoretically, this technique provides high spatial resolution measurements of wind velocity and turbulence.

1. INTRODUCTION

The winds of the atmosphere affect the performance of a variety of technologies. Adapting these technologies to the environment requires knowledge of the wind and the ability to assess risks and benefits. In performing this assessment, it is convenient to consider the wind as being composed of two parts, a steady component and a superimposed fluctuating component. The steady component can be estimated from climatological data. The fluctuating part, called turbulence, is a strongly nonlinear phenomenon. Because the details of turbulence cannot be predicted, a statistical description becomes a useful tool in this field.

Two mechanisms generate fluctuations near the earth's surface. Large Reynolds numbers generate instabilities on the air moving over a surface. The Reynolds number is defined as $\mathrm{Re} = vl/\nu$ where v is the characteristic velocity, l is the characteristic scale of flow, and ν is the kinematic viscosity of the fluid. Also mixes of warm rising

---

[1]Cooperative Institute for Research in Environmental Sciences University of Colorado, Boulder, Colorado

[2]Wave Propagation Laboratory, NOAA/ERL, Boulder, CO

air and cool descending air are generated by the solar heating of the earth's surface. As a result, electromagnetic and acoustic waves propagating through the atmosphere experience random absorption and refraction at each point along the propagation path.

Factors such as wind velocity, temperature, and humidity create random fields, which can behave as lenses. The microstructure of the refractive index of the atmosphere is determined by these factors, which can be regarded as conservative passive additives. In this case, "conservative" implies that the quantity does not change when the volume of air containing it is shifted about in space. "Passive" implies that the quantity does not affect the dynamical pattern of the turbulence (Tatarskii, 1961). The atmosphere can be conceived as a large number of random lenses of different shapes and scale sizes moving randomly through space.

An alternate representation involves the decomposition of the refractive index field into its various Fourier components. In Fig. 1.1, we consider the decomposition of a random surface wave (such as the sea surface) into its Fourier components (Pierson et al., 1955). Each Fourier component describes a two-dimensional sinusoidal modulation in the wave height that has a particular spatial wavelength and propagates in a particular direction. The actual surface is the superposition of all surface wave components of different wavelengths and propagation directions. A similar decomposition is used here for the refractive index field.

The studies of wave propagation in a turbulent medium have a direct relevance in the communications field. Designing reliable space and terrestrial high data rate communications systems requires estimates of the temporal bandwidth limitations imposed by the random

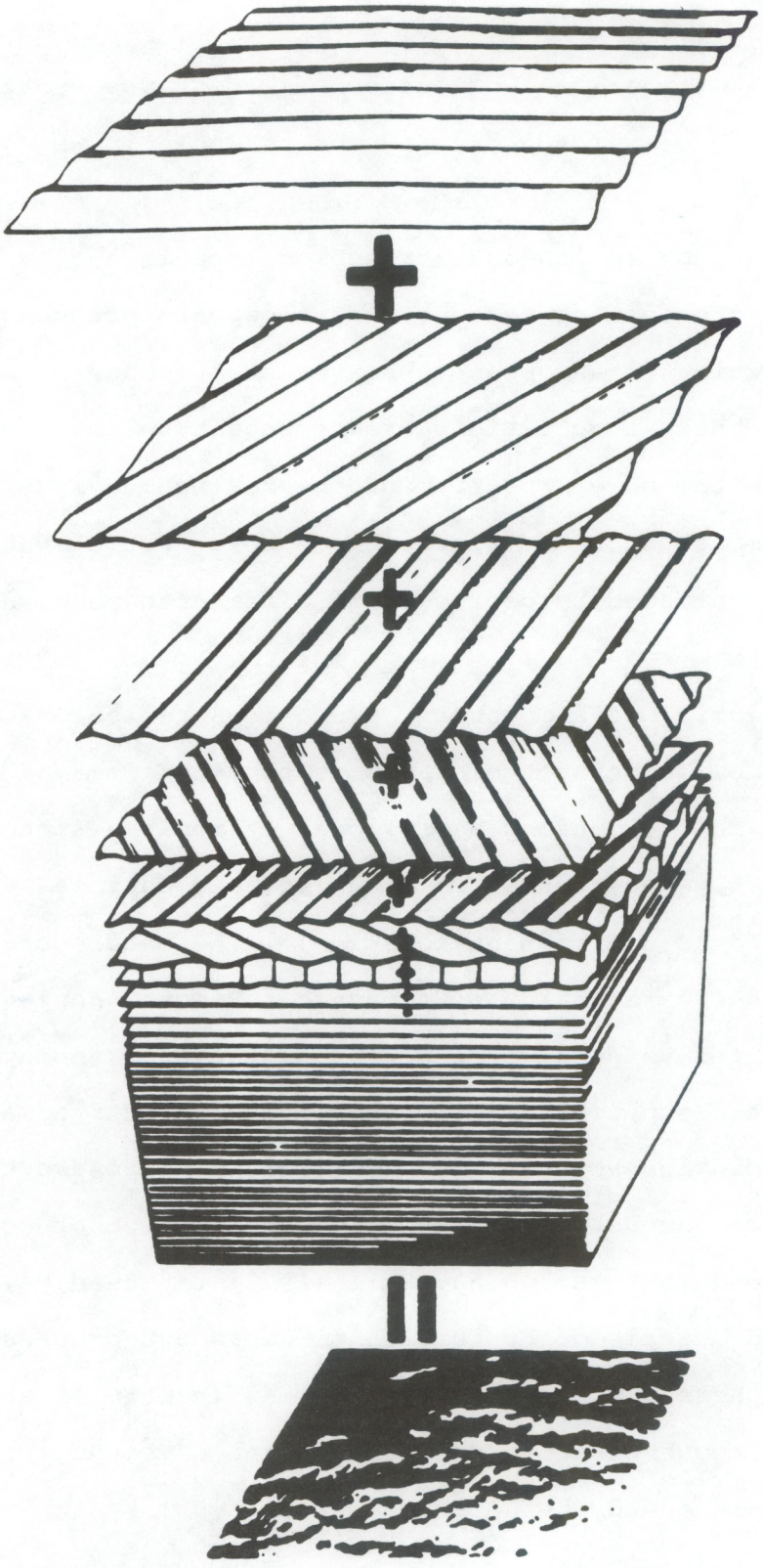

Fig. 1.1 Decomposition of a random field into its Fourier components.

atmosphere. Atmospherically induced noise degrades system performance, a main concern for achieving the potentially wide bandwidth of an optical system.

The random absorption and refraction experienced by an electromagnetic wave propagating through the atmosphere produce fluctuations in the wave amplitude and phase observed at a remote point. The statistics of these fluctuations are dependent on the geometry of the problem and on the power spectrum of the refractive index fluctuations. The impact of these fluctuations on a double-spatial filtering receiver are evaluated by performing a diffraction analysis on the system.

Remote sensing of atmospheric properties relies on the modification of waves by constituents of the atmosphere. Camagni and Sandroni (1984) define remote sensing as follows: "From the state of a field at one location, conclusions are drawn about quantities that influenced the field at a different location." The nature of the field can be electromagnetic radiation or acoustic. Remote sensing techniques can be classified as passive methods when they use radiation from natural sources (sun, earth, atmosphere) and as active methods when artificial radiation sources are used (laser, microwave transmitter).

Atmospheric acoustics involves the application of sound to atmospheric research. Brown and Hall (1978) reviewed developments in this field and described the turbulence-dependent processes in the earth's atmosphere. Winds alter the symmetric form of atmospheric layers. The frequency-dependent attenuation of sound refracted back to earth is related to the detected intensity.

Sodar, a device developed by Gilman et al. (1946), acts as an acoustic radar, where a loudspeaker transmits sound pulses upward into the atmosphere. A microphone receives scattered or reflected waves which are filtered, and a motion picture camera records the display of the received signal on an oscilloscope. The authors concluded that signal fading was a result of some unknown inhomogeneities or turbulence in the atmosphere. Later experiments improved the signal reception and attributed the attenuation of the sound waves to atmospheric inhomogeneities caused by temperature discontinuities.

Little (1969) used turbulent scattering theory and obtained quantitative estimates of the received signal strength. He used echoes for remote sensing, as well as passive sensing of natural atmospheric sounds, measurement of acoustic propagation over a path, and electromagnetic waves. He described techniques for the display of atmospheric structure, vertical profiles of wind, three-dimensional spectra of temperature and wind fluctuations, and vertical profiles of humidity. The same year, McAllister et al. (1969) used turbulent scattering theory to give a more complete description of the experimental conditions.

Recent developments in atmospheric acoustics have involved new ways to use refraction, and studies of phase and amplitude fluctuations during propagation of sound along a path. They also included insights on nonlinear effects near high-powered acoustic antennas, problems related to noise, applications dependent on the Doppler effect, and hybrid devices using both acoustic and electromagnetic waves. However, atmospheric acoustics is only useful to ranges of a few hundred meters because of the strong absorption of acoustic energy by the atmosphere. More accurate instruments are required to provide

direct quantitative data on temperature and velocity fluctuation strengths and on Doppler measured wind speeds.

Radar was first used in World War II, and has been very useful ever since as a remote sensor for atmospheric observation. Advances in technology have significantly improved the sensitivity of radar receivers; with improved satellite communications, we now have low-noise components. Microwave components at wavelengths of a few millimeters also improve sensitivity.

Kropfli et al. (1968) ran an experiment in the spring of 1966, at Wallops Island, Virginia, to determine the quantitative relationship between index of refraction fluctuations and radar reflectivity. This relationship has practical significance in the scattering of electromagnetic waves from refractive index discontinuities, which is believed to be an important mechanism for radio propagation in the troposphere.

The experiment consisted of linked mode runs in which a helicopter flew an inbound radial course from 15 to 4 n.mi while being automatically tracked by an S-band (10.7 cm) radar. The radar signal strength was measured at a fixed range increment ahead of the helicopter. The data gate was tied to the tracking gate. The intent was to measure backscattered signal strength from a region in close proximity to the tracking gate to insure that the radar and refractometer measurements were as close as possible in time and space.

The S-band is a monopulse tracking radar; it has a beamwidth of 0.5°, peak power of 3 MW, and a noise figure of 8 dB. A pulse repetition rate of 320 s^{-1} and a pulse length of 1.3 μs (650 ft) were used during these experiments. A slight correction was made to all measurements to account for receiver noise power.

The range of radar sensors can be larger than those of acoustic sensors. However, there is a poor spatial resolution associated with these ranges. In addition, radars measure fluctuations in the radar refractive index which is influenced by temperature and humidity effects. The contribution of these effects must be known in order to predict optical effects based on C_n^2 measurements.

Optical remote sensing of the earth has provided new perspectives and contributions for understanding the dynamics of the atmosphere, oceans, and the vegetation cover of the land. Examining the earth's surface via the emission or reflection of electromagnetic radiation is complicated by the intervening atmosphere. The electromagnetic energy available for passive remote sensing is obtained from the sun as reflected sunlight or re-emitted thermal radiation. An electromagnetic wave experiences scattering and absorption when it interacts with the atmosphere. The amount of energy that the atmosphere removes from or adds to the emitted or reflected wave depends on 1) the constituents of the atmosphere; 2) the path length, which is a function of the relative geometry of the source, surface, and sensor; and 3) to second order, the reflectance of the surface surrounding the scene being viewed.

Radar systems, thermal infrared devices, and optical remote sensing emerged as developments for military reconnaissance needs. The development of aerial color and color infrared photography greatly affected civilian remote sensing before 1960. Optical mechanical scanner systems became available during the 1960s and made possible acquisition of image data outside the limited spectral region of the visible and near infrared available with film. During the 1970s, the development of a new series of air and space-borne sensors stimulated

the development of the modern optical remote sensing as it is known today.

The lidar is an example of an active optical remote sensing technique. A laser pulse is fired into the atmosphere and, as it proceeds along its path, radiation is continuously scattered back toward the laser, where it is collected with a telescope and measured with a photodetector. The signal is analyzed to provide information on the magnitude of backscatter and attenuation experienced by the pulse in its passage through the atmosphere. Lasers are particularly useful because they can provide intense pulses of short duration with a narrow bandwidth and small beam divergence.

Passive optical remote sensing techniques can be applied in imaging systems, radiometric systems, and spatial filtering systems. Here we analyze a new technique in optical remote sensing of wind and turbulence using double spatial filtering of scintillation.

The concept of spatial filtering of scintillation in remote sensing was first outlined by Lee (1974). Lee was interested in profiling the transverse wind velocity and the intensity of the refractive index fluctuations along a line-of-sight using electromagnetic waves propagating through statistically homogeneous atmospheric turbulence. The spatial filtering technique described by Clifford and Lataitis (1987) and Churnside et al. (1988) relies on the one-to-one correspondence between the structure of the scintillation pattern and the scattering irregularities.

Lee (1974) proposed that turbulence intensity and spectral shape could be profiled by observing the variance of the signal for different wavelength spatial filters. Also, wind velocity could be profiled from the frequency contents of the signal under the same circumstanc-

es. The concept behind spatial filtering can be explained by decomposing the refractive index perturbations at each path position z into their transverse, two-dimensional, spatial Fourier components. Each component is characterized by a wave number $\vec{K}(z)$, as shown in Fig. 1.2a. The vector nature of $\vec{K}(z)$ and $\vec{V}_{\perp}(z)$ is dropped, and only components oriented parallel to the flow velocity are considered.

Each Fourier component acts like a thin phase screen. The intensity distribution is a magnified image of the refractive phase screen. The full scintillation pattern shown in Fig. 1.2b is the superposition of the diffraction patterns produced by all Fourier components of the refractive index at each path position.

Consider a path with a point source and a receiving aperture at opposite ends. The receiving aperture is designed so that only perturbations with a certain spatial wave number cause fluctuations in the receiver output.

The object of this method is to construct a spatial band-pass filter that is sensitive to only a single harmonic component of the scintillation pattern as it propagates across the receiving plane. It can be done by spatially modulating the amplitude or phase sensitivity across the receiving aperture. The transmitter aperture is also designed to respond to a single scale size at each path position. Thus the overall system is sensitive to only one scale size at only one path position.

A crosswind profiler (Ochs et al., 1988) was designed at the NOAA Wave Propagation Laboratory, implementing a variation of the technique proposed by Lee. The principle of this device is shown in Fig. 1.3. A pair of transmitters on the left illuminate all the receivers at the other end of the path. The receivers identify each transmitter signal

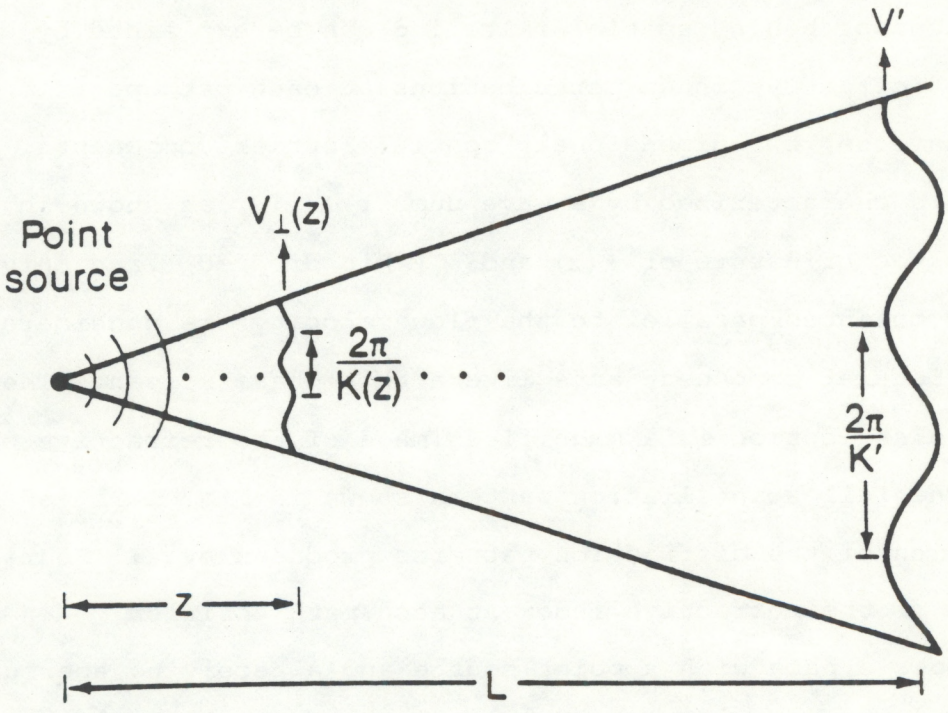

(a)

(b)

Fig. 1.2(a). Decomposition of the refractive index perturbations at each path position z. (b). Scintillation pattern.

and add them according to the signs shown. If an irregularity in refractive index carried by the wind passes across the spatial filter formed in the center of the path, it will generate a fluctuating signal in the receiver with some mean frequency. This frequency is defined as the ratio of the translation speed to the spatial wavelength of the filter. The location of the spatial filter can be altered by changing the ratio of transmitter to receiver element spacing.

A spatial-filter receiver is an incoherent receiving system with a spatially modulated aperture response. An incoherent receiver implies that its output represents the incident intensity integrated over the aperture. Spatial filters can be made by placing a mask of equally spaced opaque stripes on a lens. The mask blocks or passes sections of the incident light field. If the stripe width and space between stripes are equal, the corresponding aperture weighing function is 0 everywhere the light is blocked and 1 elsewhere. This particular filter is called nonzero-sum because the modulation function has a nonzero mean value across the aperture.

Another technique to design spatial filters uses an array of receiving elements. For example, a rectangular array of elements can be designed with an even number of columns, with a spatial wave length equal to twice the spacing between columns. This technique requires adding the intensities observed by the elements within each column. Then the net intensity of alternate columns are multiplied by -1 and the products from all the columns are added. This spatial filter is called zero-sum.

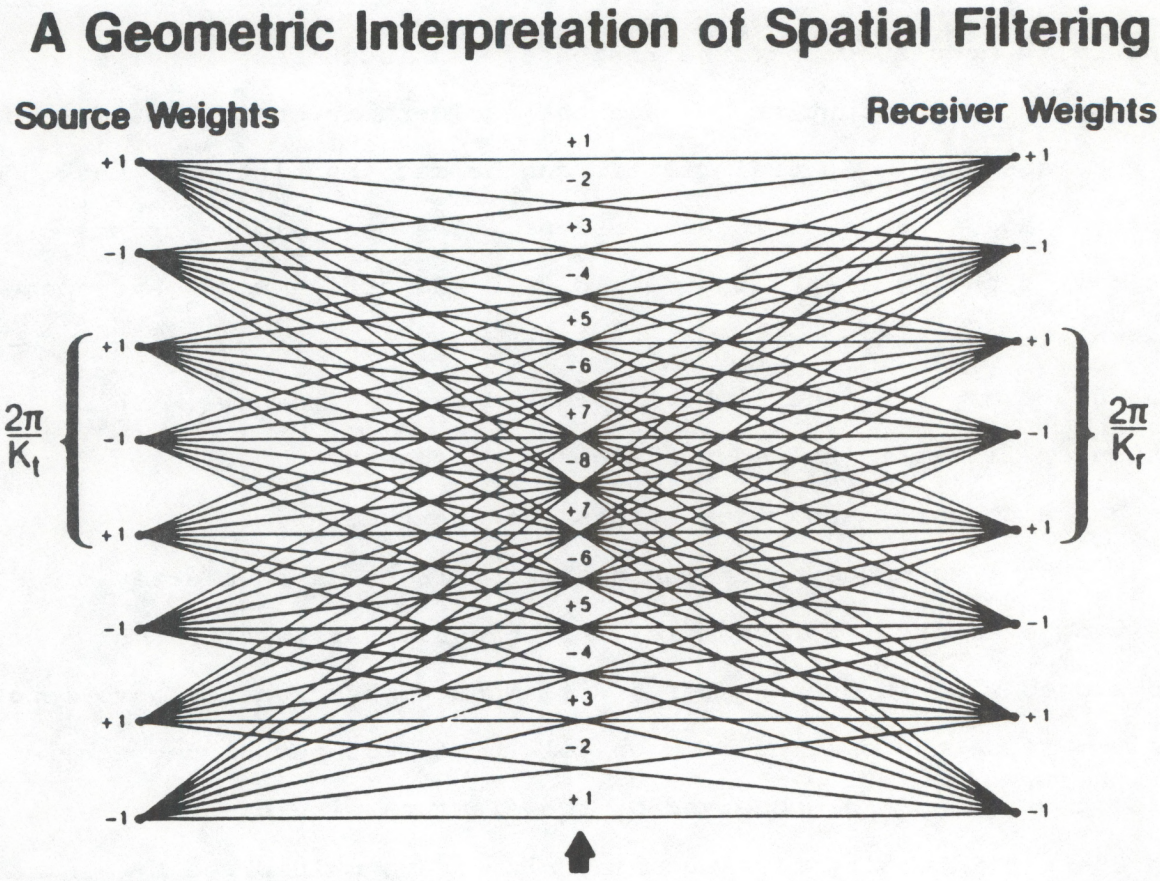

Fig. 1.3 Principles of path profiling by the use of transmitting and receiving spatial filters, first proposed by Lee.

A spatial-filter transmitter is an incoherent source with a spatially modulated aperture response. The design of the spatial-filter transmitter follows a procedure similar to the receivers requiring that the signals from each transmitter be distinguishable. It is assumed that the spatial-filter transmitters and receivers are aligned with the flow direction. Both filters imitate a sinusoidal response across the receiver aperture, as shown in Figs. 1.4 and 1.5. The orientation of the stripes of columns determines the orientation of the wave number to which the spatial filter is tuned.

2. MEASURED PROFILES OF REFRACTIVE INDEX TURBULENCE USING SPATIAL FILTERING METHODS

The simplest model of a spatial filtering system considers the contributions of the stripes and the aperture function. Two ways to separate the effects of these two sections are using a zero-sum filter and separating them in the temporal power spectrum, defined as the Fourier transform of the autocorrelation function. Evaluation of a system includes analysis of the path-weighting function. This function shows where the system is more sensitive to refractive-index fluctuations.

The system also responds to a finite region of wave-number space. Every part of the atmospheric path contributes to the scintillation pattern. In our experiment, the signal from the spatial filtering passes through a lens, which focuses it onto a light detector. The variance of the filter signal is measured, and if a zero-sum filter was used, this variance is directly proportional to the C_N^2 value. The objective of the experiment is then to infer the constant of

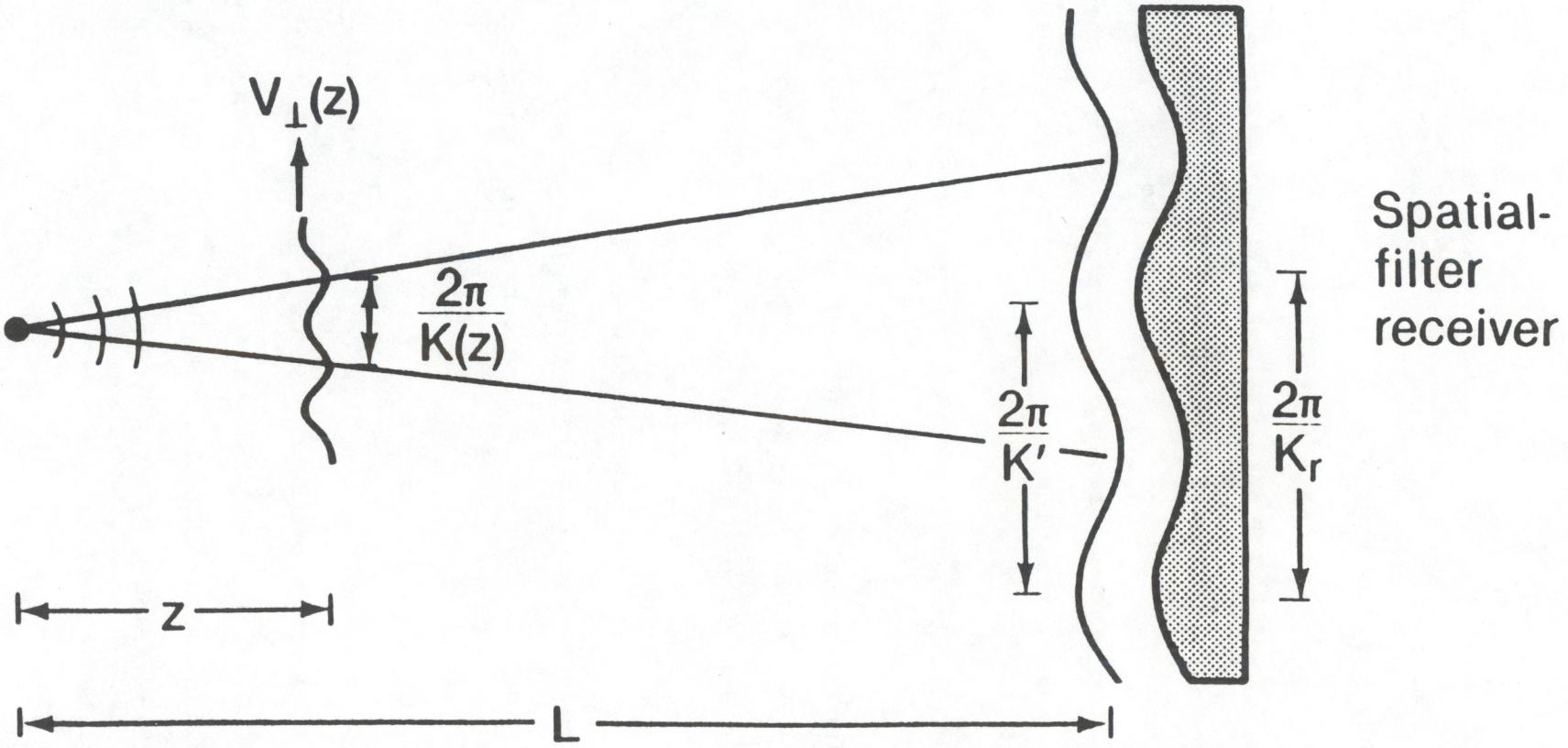

Fig. 1.4 Spatial-filter receiver

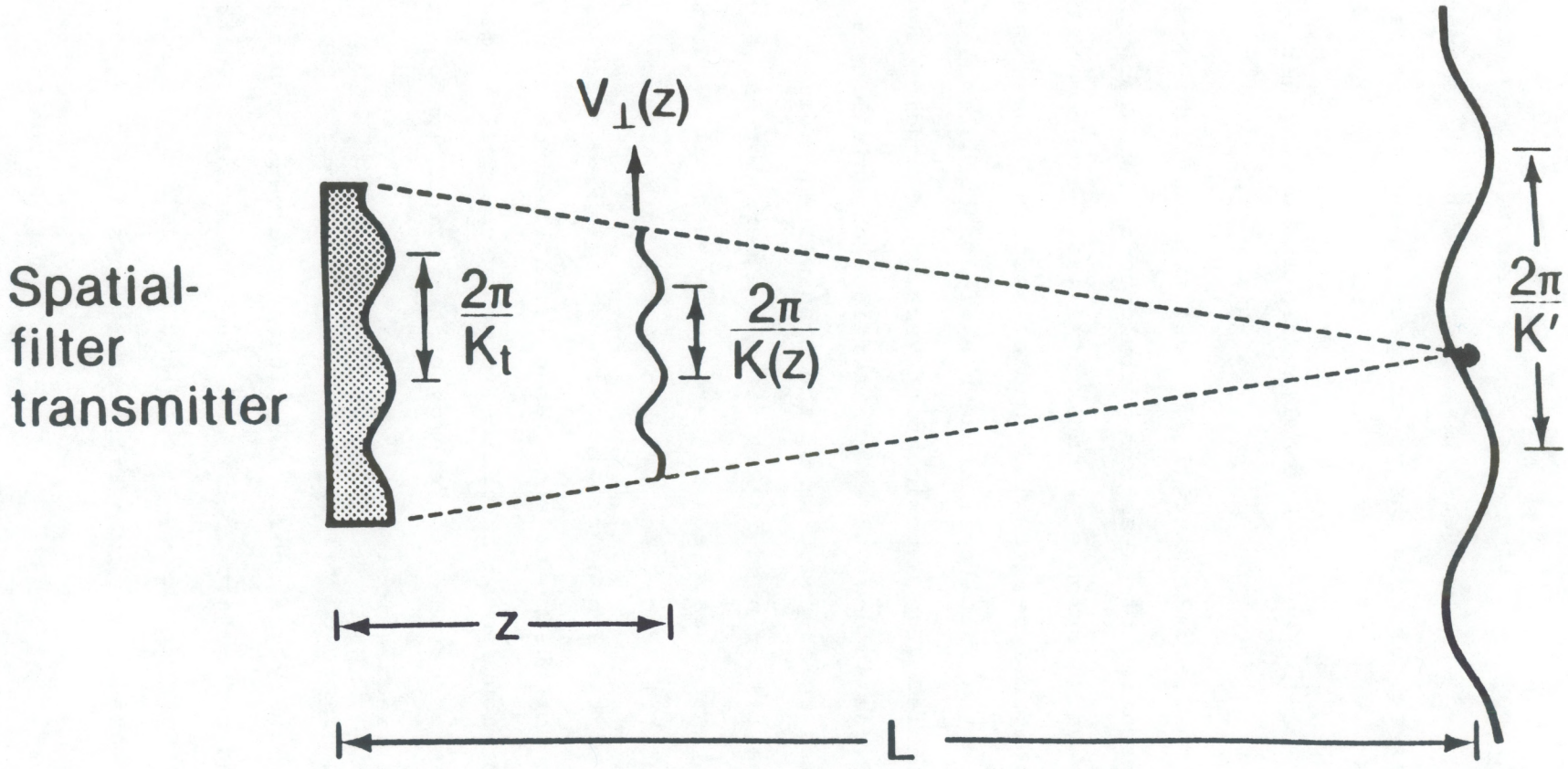

Fig. 1.5 Spatial-filter transmitter

proportionality. If a nonzero-sum filter is used, temporal filtering is required to eliminate the effects of the whole aperture. This involves calculating the power spectrum and high-pass filtering.

2.1 Two-Dimensional Spatio-Temporal Power Spectra of Stellar Scintillation

Vernin and Roddier (1973) used stellar light scintillation for remote sensing of clear-air turbulence in the troposphere. They used an improved version of Protheroe's (1964) experiment to obtain accurate bidimensional spatio-temporal spectra. These spectra clearly revealed the multilayer structure of air turbulence in the upper troposphere. The experiment of Vernin and Roddier consisted of imaging the shadow pattern on a filter of suitable transmittance and measuring power spectrum of the transmitted flux.

The filter used in Protheroe's experiment was a grating whose transmittance was a square wave, with spectral windows at frequencies 0, f, 3f, 5f, etc. The weights of the harmonics were small, and the effect of the secondary windows was neglected because of the steep decrease of the power spectrum of scintillation at high frequencies. The contribution of the zero-frequency spectral window was included to compensate for the high energy of the scintillation at very low spatial frequencies.

The improved filter in Vernin and Roddier's experiment had two complementary gratings. The fluxes observed through each grating were measured photoelectrically and then subtracted. In this way, a null average transmittance was obtained, canceling the contribution of the zero-frequency window. Figure 2.1 shows a spatial filter formed with

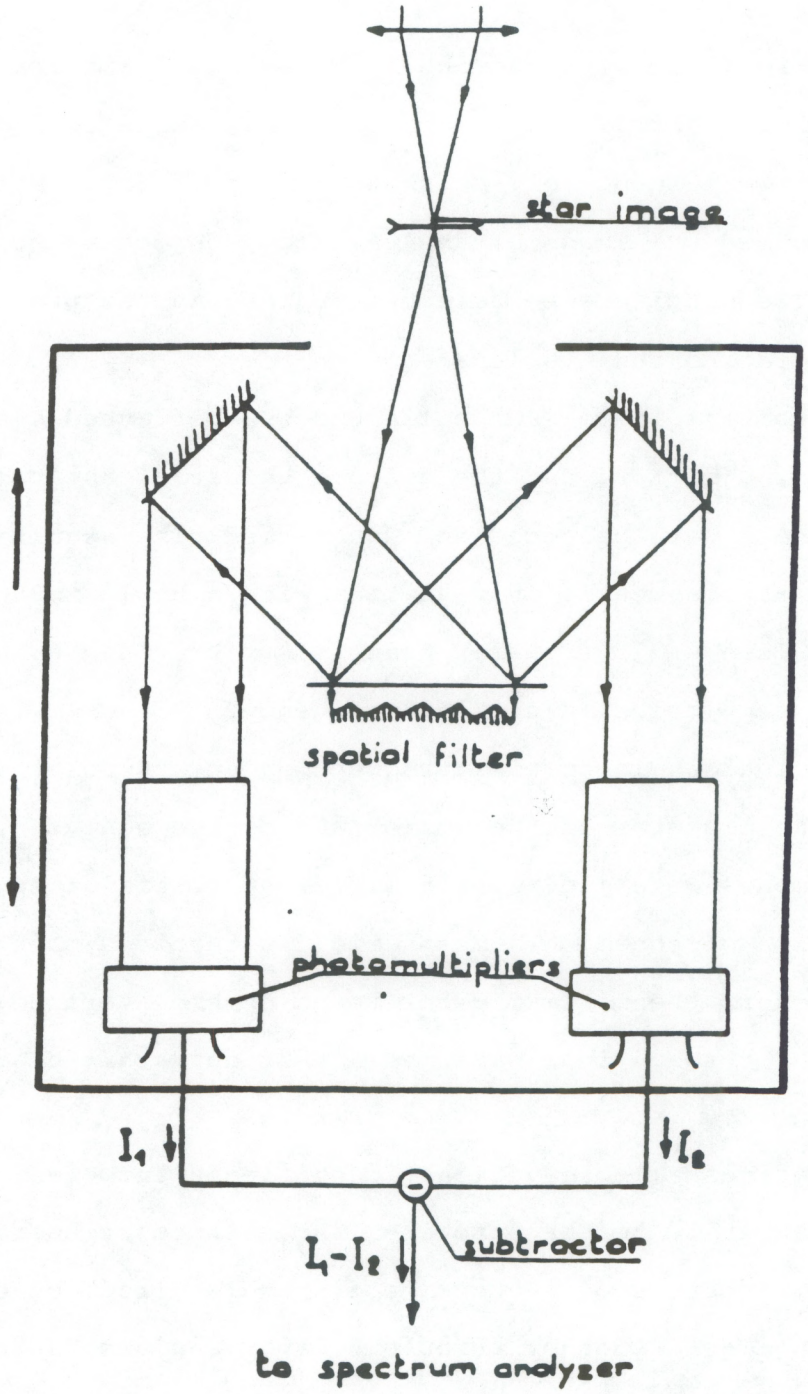

Fig. 2.1 Schematic diagram of the apparatus. The box containing the filter and the photomultipliers can move up and down and rotate around the optical axis of the incident beam, in order to select a given spatial frequency f (in modulus and direction).

a mirror grating. The arrangement in step-like formation was obtained with a stack of 26 similar glass plates at an angle of 15°, and one out of every two turned over, as shown in Fig. 2.2. A small Galilean refractor focused the image of the telescope objective on the grating. The spatial frequencies were selected by setting the proper distance between the grating and the lenses.

Two photomultipliers (PM) collected the reflected beams emerging from the grating mirror, and the average values of the corresponding electric signals were balanced and subtracted. The resulting signal was analyzed statistically in real time with a Hewlett-Packard 3721 A correlator. Then a 3720 Fourier transformer provided a temporal power spectrum for each selected spatial frequency.

The resolutions in spatial frequencies and temporal spectrum were limited by the diameter of the mirror and by the analyzer, respectively. Measurements were made for 10 different spatial frequencies, and their precision depended on atmospheric fluctuations of the turbulent energy. However, the maximum error found on the averaged values was about 20%. The observations were made on bright stars near the zenith, and mainly on ηUMa and αLyr.

The experimental observations identified a turbulent layer at an altitude of about 10 km that provided the main contribution to scintillation. The observed frequencies fitted in direction and magnitude with wind profiles. Another turbulent layer was also detected at lower and variable altitudes below 6 km. The turbulent energy of the lower layers was usually greater than that of the higher layer. However, the contributions of lower altitudes to scintillation were not as important. These results confirmed the significant contribution of a persistent turbulent layer near the tropopause.

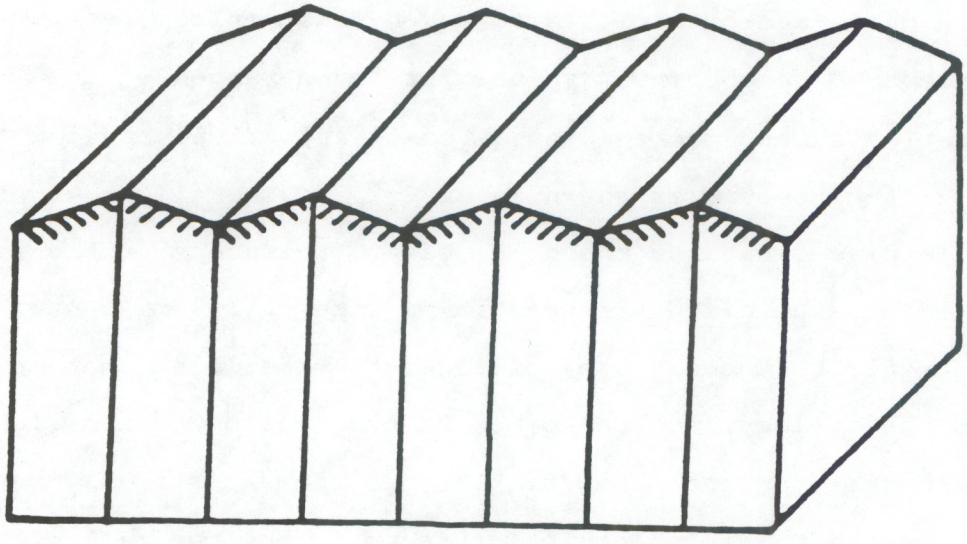

Fig. 2.2 Detail of the spatial filter, a mirror grating made of a stack of 26 similar plates.

2.2 One-Dimensional Spatial Filtering of Scintillation

Accurate observations and analysis of the twinkling of stars and motion of stellar images can provide information about turbulence and wind speed throughout the atmosphere. Ochs et al. (1976) designed a stellar scintillometer to measure refractive turbulence profiles using one-dimensional spatial filtering of scintillation. The technique measured the vertical profile of refractive-index turbulence (C_N^2) using a single star as a source and a spatial filtered detector as a receiver.

The device was a 35.6-cm Schmidt-Cassegrain telescope that focused starlight into an attached instrument package, which sequentially measured the scintillation intensity at different spatial wavelengths from 5 to 10 cm. This information was converted to electrical signals and transmitted to an on-line minicomputer. The data were processed to obtain C_N^2 values for seven ranges.

The instrument package consisted of an optical spatial filter and electronics circuitry as shown in Fig. 2.3. The filter was formed by a reticle placed outside the focus of the telescope. This reticle consisted of aluminized stripes 0.5-mm wide on 1.0-mm centers. Figure 2.3 shows two PM tubes: one collected the starlight that passed between the stripes, and the other PM tube collected the light that was reflected from the stripes. The reticle was slightly bent with respect to the telescope optical axis to direct the reflected light to the second tube by an off-axis mirror. The electrical output of one tube was subtracted from that of the other to create a spatial filter. This filter was sensitive to only one narrow band of spatial wavelengths in the scintillation pattern incident on the telescope aperture.

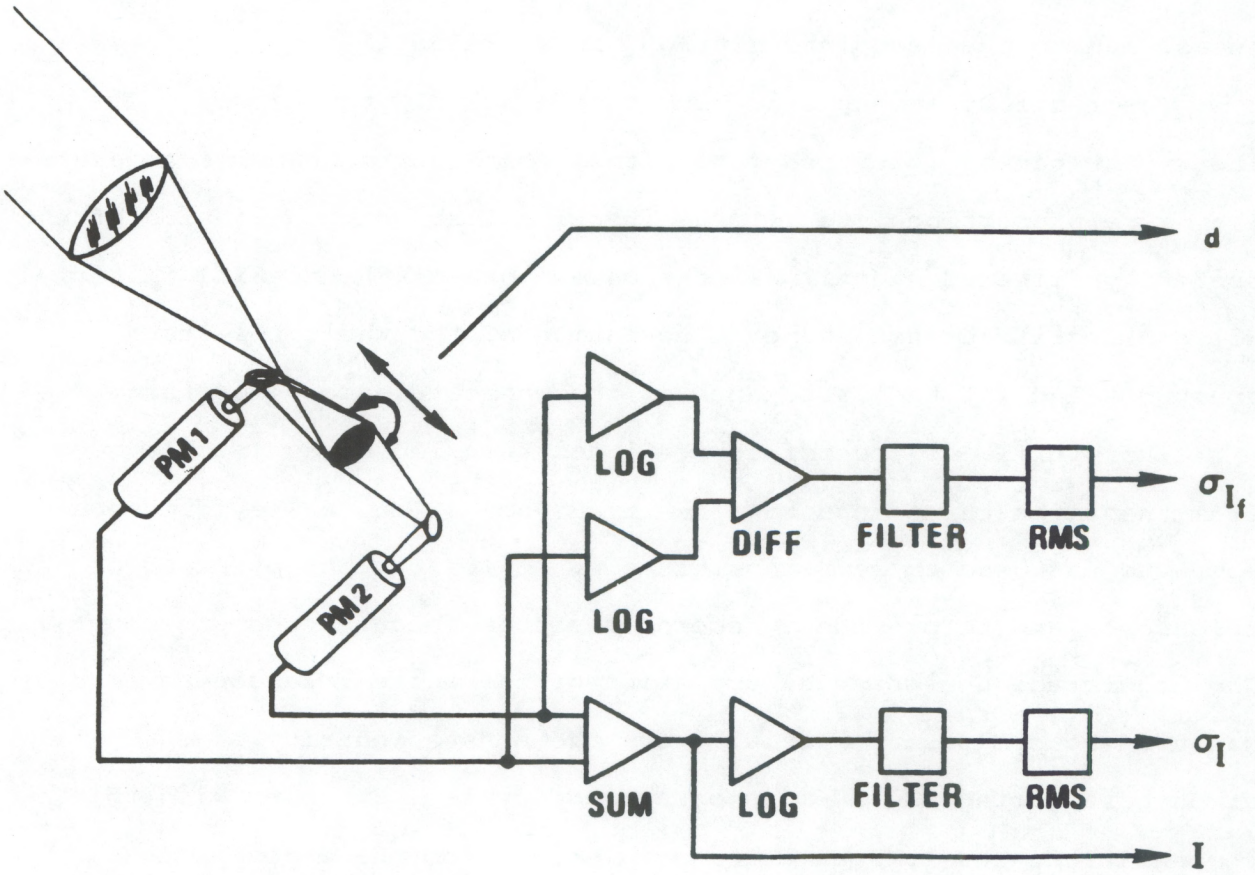

Fig. 2.3 Schematic of the optical spatial filter and the electronics.

The electrical output of the filter was a fluctuating signal whose frequency content depended on the scintillation pattern movement relative to the orientation of the filter. Therefore, the processing inferred the variance of measured quantities of the filtered intensity scintillation: the mean and the fluctuating part of the signal from both PM tubes. The electronics circuitry shown in Fig. 2.3 was designed to create a gain balance in the circuit while the reticle rotated and translated. The circuit needed to be insensitive to gain differences of the optical and electronic circuits between both PM tubes, and to the mean intensity of the starlight.

The range of atmospheric wind speeds was 0.9 to 45 m s^{-1}. The instrument package provided four signal voltages to the minicomputer. They were proportional to (1) the fractional standard deviation of the spatially filtered signal, (2) the wavelength of the spatial filter, (3) the log-irradiance standard deviation of the whole telescope aperture, and (4) the irradiance of the whole telescope aperture.

The profile of the refractive-index turbulence was calculated from the first three inputs. The irradiance of the whole telescope aperture was used to set signal levels, to monitor the pointing of the telescope, and to provide a record if clouds obscured the starlight. The log-irradiance standard deviation of the whole telescope aperture was used to compensate partially for the nonstationarity of the atmosphere during the 20-min measurement cycle. But even with this compensation, the largest error originated from the atmospheric nonstationarity.

The stellar scintillometer was designed for use with stars of second magnitude or brighter. Experimental measurements using this device were taken at Table Mountain, a mesa 12 km north of Boulder,

Colorado. The telescope was pointed to a zero-magnitude star called Vega. A quantitative comparison of the measurements obtained from the stellar scintillometer to other independent simultaneous measurements was difficult because they differ in time and location. But a self-comparison with the measured spatially filtered intensity scintillations and the variance of the whole-aperture scintillation of the telescope agreed with the results of calculated variances. The comparisons showed that the spatial filters and detectors worked as they were expected. The stellar scintillometer proved to be able to accurately measure vertical turbulence profiles if a high altitude resolution is not required.

2.3 Synthetic Aperture Spatial Filtering of Scintillation

General techniques to derive profiles of optical and radio refractive turbulence in the atmosphere have used in situ and remote sensors. In situ sensors provide very high spatial resolution, but they cannot provide data continuity in time. Remote sensors do not have as high resolution as in situ sensors, but they do provide almost continuous monitoring of the atmosphere with minimum expense. The technique (Clifford and Churnside, 1987) of using synthetic aperture spatial filtering of scintillation was designed to combine the good features of in situ and remote sensor methods.

The geometry of the synthetic aperture spatial filter concept is shown in Fig. 2.4. An elevated point source of light moves across the field of view of a passive optical system on the ground. The light source can be on an airplane designed for this purpose or on remotely piloted vehicles. Other designs use tower-mounted or balloon-borne

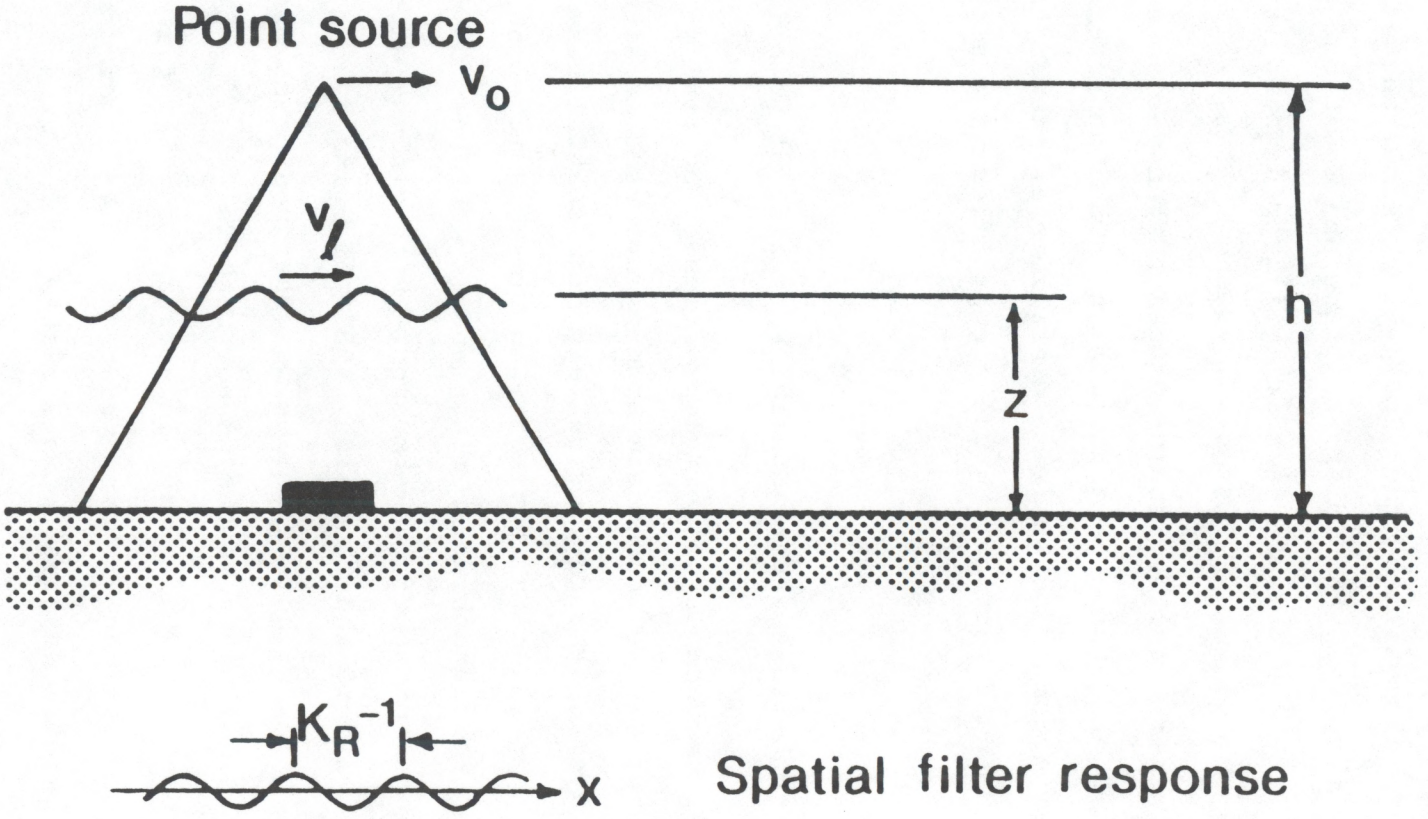

Fig. 2.4 Synthetic aperture spatial filtering geometry.

retroreflector arrays. In all these examples, the ground system requires a scanning laser to simulate the translation velocity. In any case, the source speed must be faster than the atmospheric motion between the source and the ground.

The principle behind this technique is that the light source moves across the field of view of a receiver array on the ground. As the wave propagates downward, it confronts a moving refractive turbulence irregularity, which behaves as a phase-perturbing screen. The source has an assigned wave number as a function of the wavelength, at a height h above the ground. As the source is moving with a velocity v_s in the horizontal plane, the wave confronts an irregularity of a certain wave number at a height z. The parameter v_1 in the scheme represents the velocity of the single phase screen. Clifford and Churnside (1987) used spatial and temporal filtering of the signal from a moving source to retrieve the spectrum of the refractive-index fluctuations at a specific path position.

Figure 2.5 shows how a spatial filter senses the turbulent medium. A spherical wave propagates through the atmosphere from z=h to z=0, and the turbulent irregularities that it encounters perturb its phase front. Eventually, at the ground level, fluctuations in the scintillation pattern will exist at nearly all spatial wave numbers. The scintillation pattern is the received irradiance as a function of position on the ground. The spatial filter receiver responds to some finite resolution cell in both wave number and path position, rather than the expected single wave number at a single path position. This fact, plus the effects of a certain amount of unavoidable noise, limits the precision of the measurements.

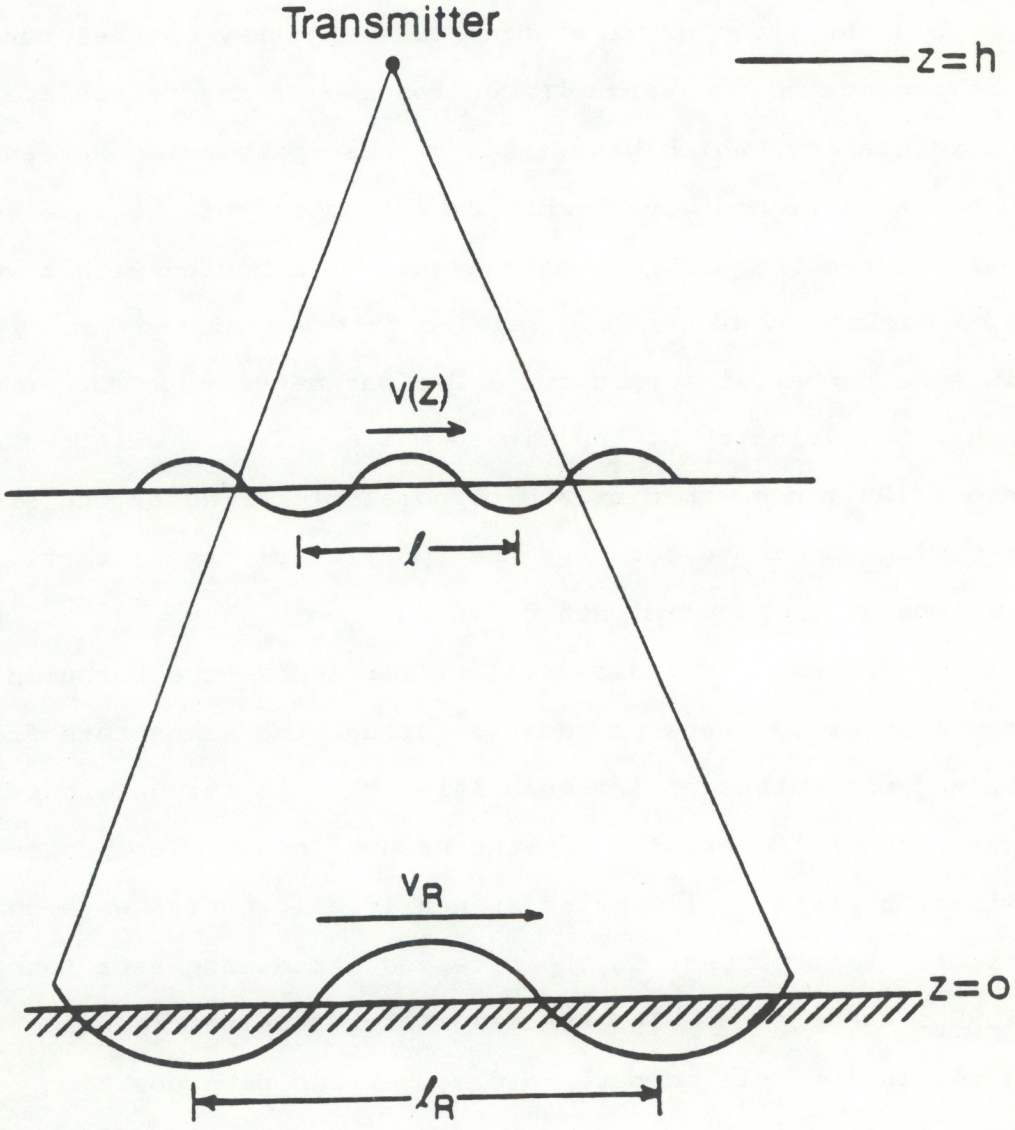

Fig. 2.5 Effect of a single component of turbulence on the received irradiance.

The limits of resolution and precision vary for several system configurations, such as zero-sum filters, nonzero-sum filters, and multiple aperture systems. For these systems, it is assumed that the receiver rather than the source limits the resolution. This assumption implies that the synthetic aperture spatial filter created by the moving source must contain more cycles than the receiver spatial filter. The accuracy in the estimated power spectrum limits the precision of the measured C_N^2 . This accuracy depends on the fluctuations of the signal during the measurement time and on the effects of receiver noise.

In a zero-sum receiver, shown in Fig. 2.6, an aperture of certain radius collects the incident light. The spatial filter behind the aperture consists of reflective stripes alternating with equal width transmissive stripes. One photodetector collects the light transmitted by the filter, a second detector collects the reflected light. The difference between these two detector outputs is fed into a spectrum analyzer to provide turbulence strength as a function of height. The effective frequency of the spatial filtering can be adjusted to sample different regions of the turbulence spectrum. One way is to place optical magnification in front of the filter.

A nonzero-sum receiver is composed of a single detector and a spatial filter that transmits alternate stripes. The receiver uses only one-half the optical power incident on the aperture. However, the weighting functions and the bias in the estimate of C_N^2 are the same for both zero-sum and nonzero-sum receivers. The precision in the estimated measurements of C_N^2 is the same for both receivers at high signal-to-noise ratios. At lower ratios, the precision for the nonzero-sum receiver is equivalent to that for the zero-sum with 3-dB

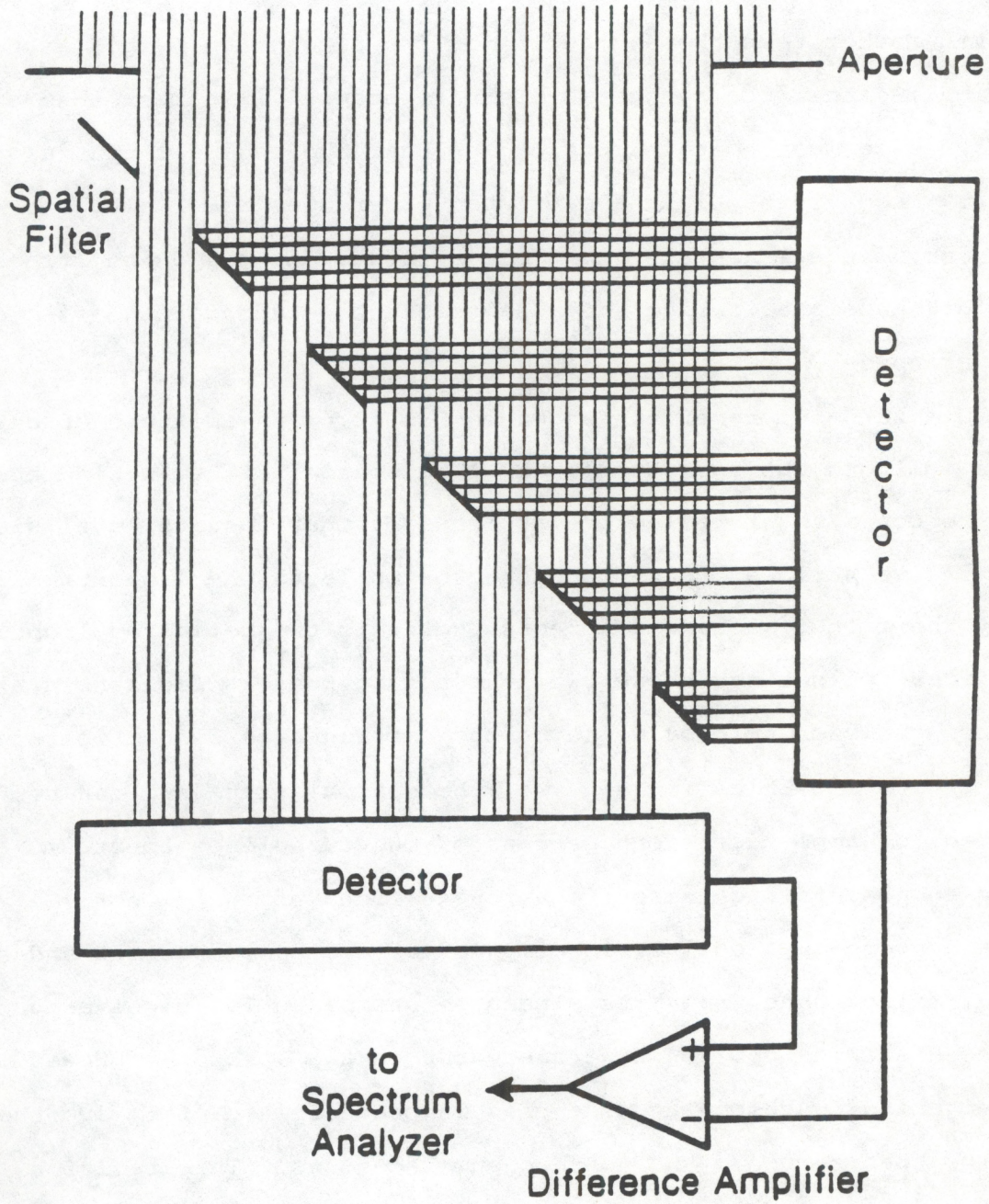

Fig. 2.6 Schematic diagram of single-aperture zero-sum receiver.

less signal-to-noise ratio at each detector. The zero-sum receiver approximates most closely the ideal, but the nonzero-sum receiver is much simpler to implement.

A multiple aperture system consists of an array of small detectors, each with its own preamplifier. The outputs from these detectors are summed electronically, and different combinations of them can generate the filter function for the zero-sum or the nonzero-sum receiver. For example, a zero-sum receiver is formed when the signals from alternate detectors are inverted before summing.

A hypothetical example involving this technique uses a 5 mW He-Ne laser source, with 100 mrad of beam divergence mounted on a light plane flying at 100 m s^{-1} at a height of 1 km. The receiver array located at the ground level consists of 10 detectors separated by 1 m. Each detector is formed of a 10-cm diameter telescope with 100-mrad field of view followed by a 1-nm optical bandpass filter and photodiode. The system is operating at a frequency of 50 Hz and a correspondent bandpass of 10 Hz.

The conditions are established to measure the turbulence at 500 m above the ground. The theoretical spatial solution implies that the measurement represents an average of the turbulence between 400 and 600 m. In the ideal system evaluation, a typical value of

$$C_N^2 = 10^{-16}\ m^{-2/3}$$

at 500 m tests the measurement bias. The analytical results suggest that the uncertainty in the measurement is dominated by noise if C_N^2 is less than 4.5×10^{-17}. For values of C_N^2 greater than 4.5×10^{-17}, there is an rms uncertainty of about 18%. Therefore, profiles of refractive turbulence strength and spectral slope can be obtained by

spatially and temporally filtering the scintillation pattern observed at ground level.

2.4 High-Resolution Optical Spatial Filter System

A technique developed by Churnside et al. (1988) achieved high-resolution profiles of C_N^2 using an optical spatial filter system. The technique provides high spatial resolution measurements of refractive turbulence along a line of sight, as shown in Fig. 2.7. The system consisted of a spatially filtered optical transmitter and a spatially filtered optical receiver at opposite ends of the path. The corresponding path and wave-number weighting functions describe the sensitivity of the system to different path positions and spatial wave numbers of the refractive turbulence spectrum.

Analysis of this system begins by inferring analytic expressions for the path and wave-number weighting functions in terms of known parameters from idealized approximations to the modulation functions. Then, analytic results and approximate functions for the corresponding temporal spectra are derived and compared to numerical solutions for more realistic functions. The characteristics of the spatial filters can be modified by filtering the temporal spectrum of the spatially filtered signal. Consequently, these temporal spectra lead to high-resolution profiles of C_N^2 .

Covering the source and the receiver aperture with equally spaced parallel strips of tape generated a nonzero-sum spatial filter with a modulation function of 0 everywhere there was a strip of tape, and 1 elsewhere. The distance between the centers of the strips of tapes defined the spatial filter wavelength. This simple spatial filter cannot be used for all applications in remote sensing. Its response

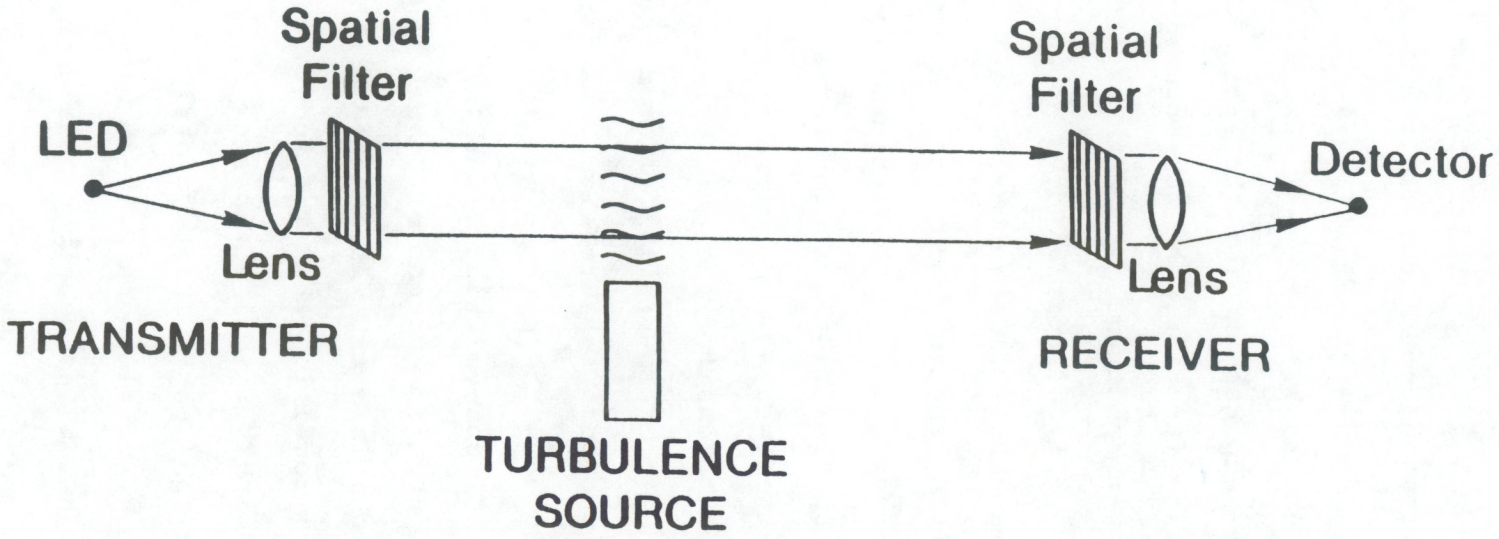

Fig. 2.7 Schematic diagram of experiment configuration.

has two components, one resulting from an unmodulated aperture and another from a modulated zero-sum aperture. More complex spatial filters require that the transmitted signals are coded so that the intensity from adjacent stripes on a source can be subtracted. The same procedure follows for the receiver requiring more elaborate signal processing.

Complex expressions for the spatial power spectrum lead to the path-weighting function, the wave-number-weighting function, and the temporal power spectrum. The path-weighting function is the sum of four terms: (1) the spatial dc component of the modulation functions, (2) the component from a zero-sum spatial filter source and an unmodulated receiving aperture, (3) the component from a zero-sum spatial filter receiver and an unmodulated source, and (4) the component from a zero-sum spatial filter source and spatial filter receiver.

Some experimental observations were done to measure several weighting functions for the particular geometry shown in Fig. 2.7. A source transmitted spatially filtered incoherent light across a 110-m flat grassland path to a receiver. A narrow turbulence source was moved up and down the path to measure the weighting function. The source was a light-emitting diode (LED) operating at a wavelength of 0.93 μm, a junction current of 0.55 A, and an estimated output power around 40 mW. This LED was located at the focus of a Fresnel lens with a 40-cm focal length. The spatial filter in the configuration was formed with vertical stripes of tape on a piece of acrylic plastic in front of the lens. The tape stripes were 1.27 cm wide with 1.27 cm of separation, obtaining a 2.54-cm wavelength for the spatial filter.

The light at the receiver passed through three separate spatial filters with spatial wavelengths of 1.52, 2.54, and 15.2 cm. The light

was then collected by a circular lens with a 1-m focal length and a 22.2-cm diameter. The collected light went through an interference filter to block background light and into a silicon photodiode. The interference filter had a bandpass of 60 nm centered at an optical wavelength of 940 nm. The detected signal went through a process of amplification, filtering, and digitization.

The turbulence source was a 44-kW kerosene heater blowing hot air through a 23-cm-diameter barrel. A fine platinum wire was used to measure the turbulence characteristics of the heater. Since the resistance of the wire depends on its temperature, a small current was induced through it and the resulting voltage drop was received by the analog-to-digital converter of a computer. This signal was digitized, and the resulting spectrum showed the finite temporal response of the probe to fast changes in temperature. The refractive index fluctuations were calculated as a function of pressure, temperature, measured temperature structure, and spatial separation. The estimated value for C_N^2 was 3×10^{-10} $m^{-2/3}$ and did not consider the fluctuations caused by concentrations of kerosene vapor and combustion products.

The system was also tested under natural turbulence conditions. Data sets were recorded using a 2.54-cm spatial filter at the receiver. The variances of the signal were compared with those from an incoherent optical scintillometer, which provided C_N^2 values averaged over a 250-m path parallel to the path of the experiment. A linear relationship was found between these variances and the refractive index fluctuations. The proportionality constant generally depends on the aperture geometry, propagation path length, and optical wavelength. The results achieved good correlation with independently

measured values of turbulence strength, proving the feasibility of this technique.

3. DOUBLE SPATIAL FILTERING SCINTILLATION TECHNIQUE

The previous sections introduced the concept of optical remote sensing using spatial filtering techniques. These techniques are used to measure the strength of refractive turbulence at some localized region between the transmitter and receiver, and/or cross-wind velocity. The technique proposed by Lee requires a spatial filter on each side of the measured volume. This implies the use of a spatially filtered transmitter in space for the case of vertical profiles of the atmosphere.

The techniques developed for the stellar scintillometer using a passive source to measure vertical profiles show a poor resolution. Some information is lost when the transmitter is not spatially filtered. Profiles of turbulence strength can be obtained optically, however some other devices must compensate for the missing information when measuring wind profiles.

This section introduces a new technique involving two spatial filters at the receiver end of the path, and an arbitrary transmitter. Theoretically, this technique provides high spatial resolution measurements of wind velocity and turbulence. The transmitter can be any natural or artificial source: a laser, a thermal source, the sun, the moon, or a star, among others.

3.1 Geometrical Analysis

The geometrical analysis represents the ideal conditions for a double spatial filtering technique. Its general operation is described by using a ray tracing approach (Churnside et al., 1990). Hypothetically, light originating at a distant source propagates through the atmosphere and is scattered by each Fourier component of turbulence. The ray diagram of Fig. 3.1 shows the ray paths that are scattered by one such component and pass through the clear regions of the spatial filters.

Two spatial filters, labeled G_1 and G_2, at the receiving end of the path are formed with clear and opaque regions of equal width. The distance s represents the separation between filters. A periodic scattering structure T with a period of λ_T is assumed at a height h above the receiver. This constitutes one Fourier component of the random refractive index field called refractive turbulence.

Two adjacent rays start at one cycle of the scattering structure. The rays are separated by λ_1 at a distance h, and by λ_2 at a distance $h+s$; λ_1 and λ_2 represent the periods of gratings G_1 and G_2, respectively. The angle between the two rays is θ . Assuming $\theta \ll 1$ rad, it can be observed that

$$\theta = \frac{\lambda_1}{h} = \frac{\lambda_2}{h+s}. \tag{3.1}$$

As shown in the diagram, the two adjacent rays merge at one cycle of G_2. These rays are separated by λ_1 at a distance s in front of that grating, and by λ_T at a distance $h+s$. Denoting as ϕ the angle between these two rays, it is observed that

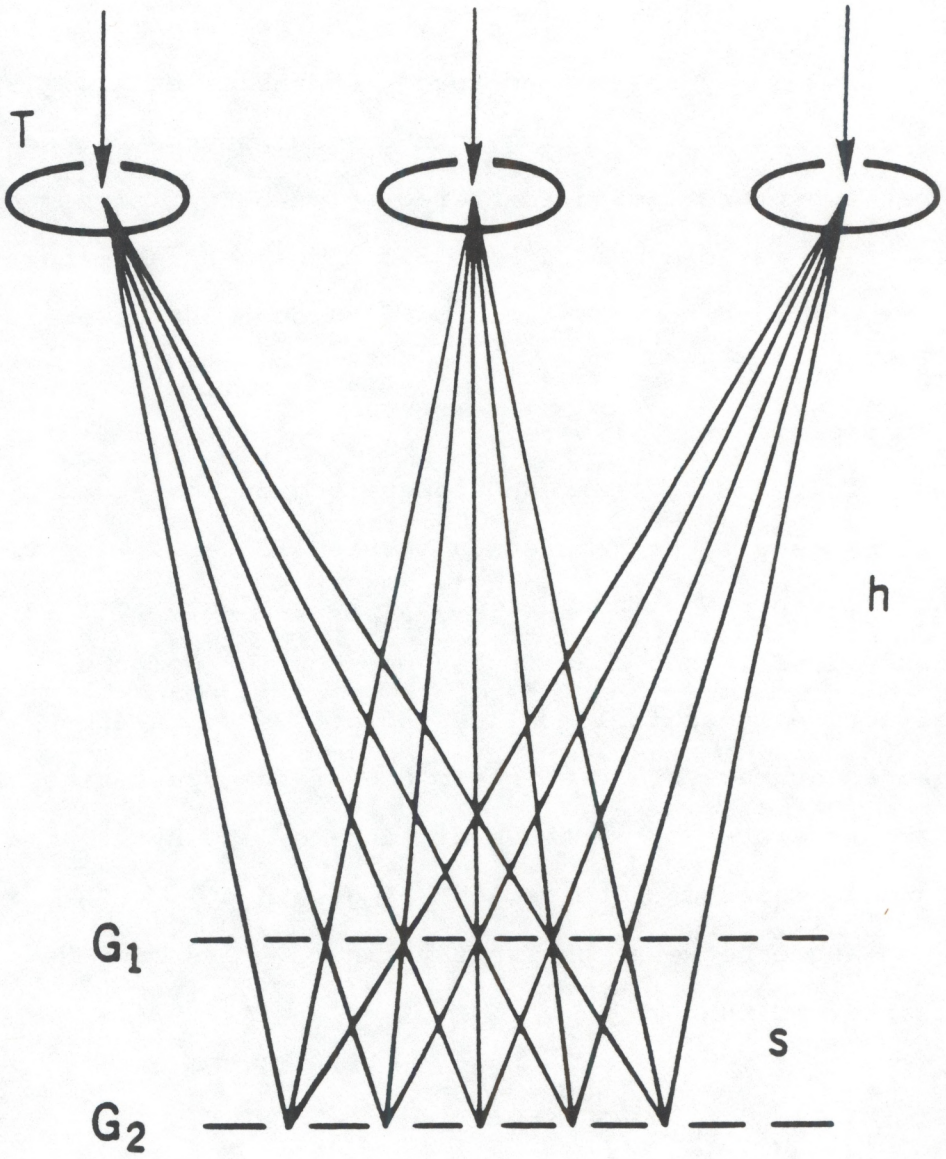

Fig. 3.1 Ray diagram for double-spatial-filter configuration showing turbulent scattering layer (T) at distance h and the two receiver gratings (G_1 and G_2) separated by distances s.

$$\phi = \frac{\lambda_1}{s} = \frac{\lambda_T}{h+s}. \qquad (3.2)$$

Defining K as the wave number $2\pi/\lambda$ corresponding to each period λ, and relating the two conditions above, it is inferred that the wave number at the scattering particle is given as the difference between the wave numbers of gratings G_1 and G_2.

From equation (3.1),

$$h = \frac{s\lambda_1}{\lambda_2 - \lambda_1}.$$

From equation (3.2),

$$\lambda_T = \frac{\lambda_1 (h+s)}{s}$$

$$K_T = \frac{2\pi}{\lambda_T} = \frac{2\pi s}{h\lambda_1 + s\lambda_1} = \frac{2\pi s}{\left(\frac{s\lambda_1}{\lambda_2 - \lambda_1}\right)\lambda_1 + s\lambda_1}$$

$$= \frac{2\pi s(\lambda_2 - \lambda_1)}{\lambda_1^2 s + s\lambda_1(\lambda_2 - \lambda_1)} = \frac{2\pi(\lambda_1 - \lambda_2)}{\lambda_1 \lambda_2}$$

$$= \frac{2\pi\lambda_2 - 2\pi\lambda_1}{\lambda_1\lambda_2} = \frac{2\pi}{\lambda_1} - \frac{2\pi}{\lambda_2},$$

and, by definition,

$$K_T = K_1 - K_2$$

$$K_T = \frac{2\pi}{\lambda_T} = \frac{2\pi s}{\lambda_1 (h+s)} = \frac{2\pi s}{\left(\frac{\lambda_2 h}{h+s}\right)(h+s)} = \frac{2\pi s}{\lambda_2 h}. \qquad (3.3)$$

Therefore, the height h is given by

$$h = \frac{2\pi s}{\lambda_2 K_T} = \frac{\left(\frac{2\pi}{\lambda_2}\right)s}{K_T}$$

$$h = \frac{K_2}{K_1 - K_2} s \quad . \tag{3.4}$$

3.2 Spatial Resolution of a System

The spatial resolution of a system is defined as the length of the measurement volume. Consider a receiver aperture of diameter D that contains N_1 cycles of grating G_1, so $D = N_1 \lambda_1$. Figure 3.2 shows the spatial resolution Δh of the system. Consequently, the upper and lower limits of the measurement volume are located at $h \pm 1/2\,\Delta h$.

Observing again Fig. 3.1, note that rays from a point at height h over the receiver project an image of G_1 onto G_2 with the same period as grating G_2. But rays originating above h project an image of G_1 onto G_2 with shorter periods. As a result, the system response is reduced. Therefore, the upper limit of the measurement volume is defined as the scattering height at which the phases of the projection of G_1 onto G_2 and G_2 differ by one-half cycle over the aperture diameter. A similar definition applies to the lower limit.

Following a similar analogy, as in equation (3.1), the angle between adjacent rays from the upper and lower limits is given by

$$\theta\pm = \frac{\lambda_1}{h \pm 1/2\,\Delta h} = \frac{\lambda_2\,[1 \mp 1/(2N_1)]}{h \pm 1/2\,\Delta h + s} \quad , \tag{3.5}$$

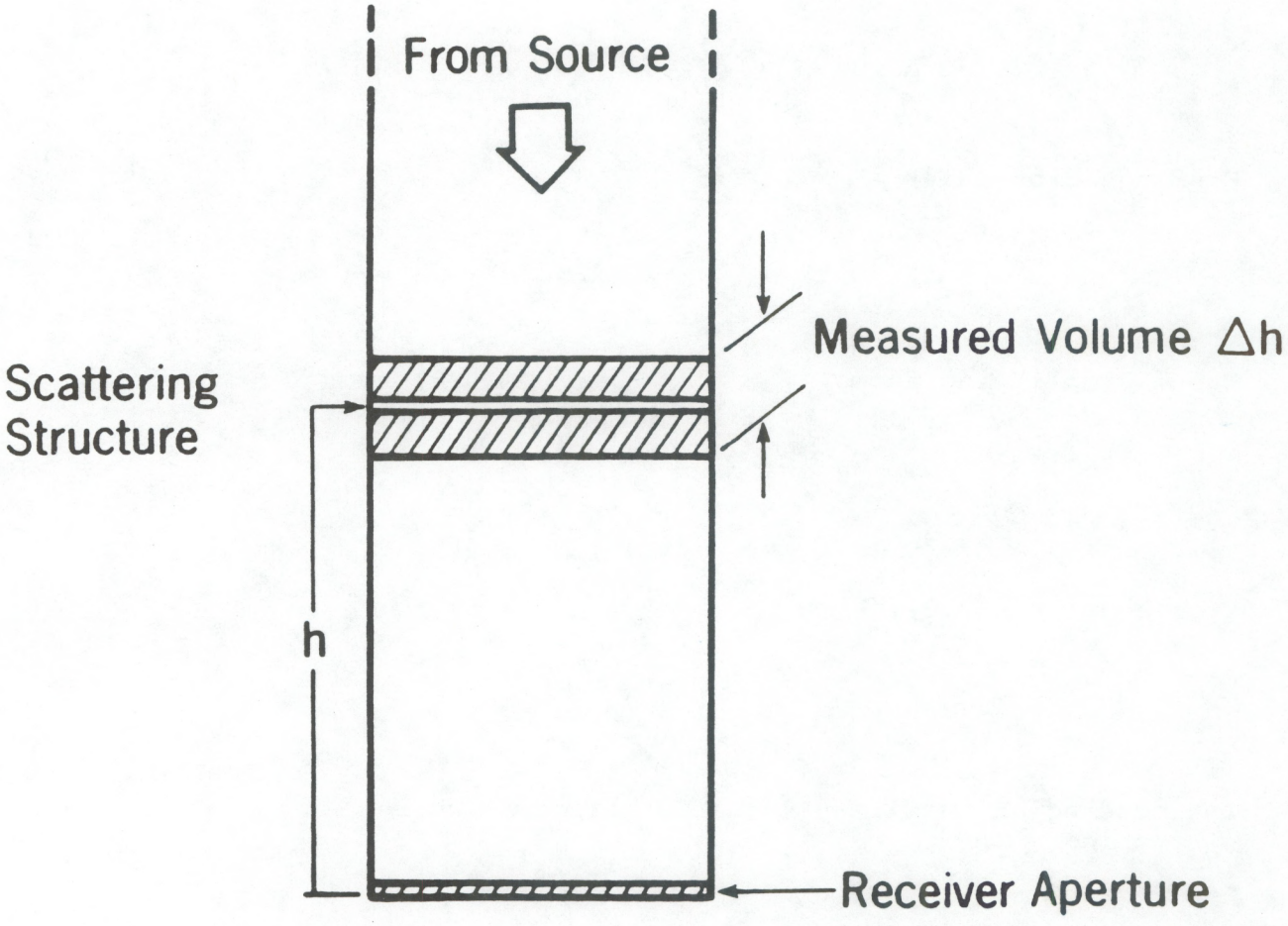

Fig. 3.2 Schematic diagram of the measured volume Δh

where the upper and lower signs correspond to the upper and lower limits, respectively.

Solving for the spatial resolution, from equation (3.5),

$$\lambda_1 (h \pm 1/2\ \Delta h + s) = \lambda_2 (h \pm 1/2\ \Delta h) \left(1 - \frac{1}{2N_1}\right) .$$

Gathering terms, and developing for the upper limit,

$$1/2\ \Delta h \left(\lambda_1 - \lambda_2 + \frac{\lambda_2}{2N_1}\right) = \lambda_2 h \left(1 - \frac{1}{2N_1}\right) - \lambda_1 (h+s)$$

$$1/2\ \Delta h \left(\lambda_1 - \lambda_2 + \frac{\lambda_2 \lambda_1}{2D}\right) = -h \left(\lambda_1 - \lambda_2 + \frac{\lambda_2 \lambda_1}{2D}\right) - \lambda_1 s \quad .$$

From equation (3.4),

$$h = \frac{\lambda_1}{\lambda_2 - \lambda_1}\ s \quad .$$

Then, simplifying terms,

$$1/2\ \Delta h = -h - \frac{h(\lambda_2 - \lambda_1}{\lambda_1 - \lambda_2 + \left(\frac{\lambda_2 \lambda_1}{2D}\right)} \quad .$$

From equation (3.3),

$$\lambda_2 = \frac{\lambda_1 \lambda_T}{\lambda_T - \lambda_1} \quad .$$

Introducing an auxiliary variable called A, where

$$A = \frac{\lambda_2 - \lambda_1}{\lambda_1 - \lambda_2 + \left(\frac{\lambda_2 \lambda_1}{2D}\right)}$$

and substituting the value of λ_2,

$$A = \frac{\left(\frac{\lambda_1 \lambda_T}{\lambda_T - \lambda_1}\right) - \lambda_1}{\lambda_1 - \left(\frac{\lambda_1 \lambda_T}{\lambda_T - \lambda_1}\right) + \frac{\left(\frac{\lambda_1 \lambda_T}{\lambda_T - \lambda_1}\right) \lambda_1}{2D}} \quad .$$

This expression reduces to

$$A = \frac{2D}{\lambda_T - 2D} \quad .$$

Substituting this expression into the spatial resolution equation,

$$\pm 1/2 \, \Delta h = -h - h\left(\frac{2D}{\lambda_T \pm 2D}\right) = \frac{-h\lambda_T}{\lambda_T \pm 2D}$$

$$\pm 1/2 \, \Delta h = \frac{\pm \left(\frac{\lambda_T h}{2D}\right)}{1 \mp \left(\frac{\lambda_T}{2D}\right)} \quad . \tag{3.6}$$

If we define N_T as the number of cycles of the difference grating across the aperture $N_T = D/\lambda_T$,

$$1/2 \Delta h = \frac{\left(\frac{\lambda_T h}{2D}\right)}{1 - \left(\frac{\lambda_T}{2D}\right)} = \frac{\left(\frac{h}{2} \cdot \frac{1}{N_T}\right)}{1 - \left(\frac{1}{2} \cdot \frac{1}{N_T}\right)}$$

$$1/2 \Delta h = \frac{h}{2N_T - 1}$$

$$\frac{\Delta h}{h} = \frac{1}{N_T - \frac{1}{2}} \quad .$$

Assuming $N_T >> 2$, finally,

$$\frac{\Delta h}{h} \approx \frac{1}{N_T}. \tag{3.7}$$

3.3 Wave Number Resolution of a System

The system is designed to be sensitive to one two-dimensional Fourier component of the refractive index. The wave-number resolution ΔK_T contains the upper and lower limits of the range of wave numbers to which the system responds. This range is defined by $K_T + 1/2\ \Delta K_T$. Assuming N_T cycles of K_T wave numbers across the aperture, $K_T + 1/2\ \Delta K_T$ produces $N_T + 1/2$ cycles and $K_T - 1/2\ \Delta K_T$ produces $N_T - 1/2$ cycles. Following an analysis similar to that of the previous section,

$$\frac{\Delta K_T}{K_T} = \frac{1}{N_T}. \tag{3.8}$$

The double spatial filtered receiver responds to turbulence with a wave number that is the difference of the receiver spatial filter wave numbers and is located at a height given by the ratio of the receiver filter separation and the fractional difference in the filter wave numbers. The fractional height resolution equals the inverse of the number of cycles of the receiver difference wave number across the aperture.

3.4 Wind Velocity

The wind velocity can be inferred by observing the turbulence that sweeps past the receiver with the wind. A turbulent wave number K_T generates an angular frequency out of the receiver of $\omega = v K_T$, where v is the velocity component parallel to K_T. In the absence of velocity fluctuations and detector noise, the spectral width is calculated from the range of wave number values $(\Delta \omega/\omega = 1/N_T)$. The uncertainty in the velocity estimate is related to the spectral width $(\Delta v/v = 1/N_T)$.

3.5 Telescope Effects

A telescope can improve the system when two spatial filters are placed behind it. In this way, the light is collected over a large area. Figure 3.3 shows an schematic diagram of the geometry: two lenses L_1 and L_2, two gratings G_1 and G_2, and two projected images of the gratings G_1' and G_2'. The objective of this analysis is to infer the characteristics of the projected image of the gratings, because they provide the spatial filtering of the incoming light.

The two gratings G_1 and G_2 are separated by a distance s. The two lenses in the telescope L_1 and L_2 have focal lengths f_1 and f_2, respectively, and they are separated by a distance b. The telescope is located at a distance d from the gratings. The information required from the two image gratings consists of the separation between them, and the effective grating constants K_1' and K_2'.

The positions of G_1' and G_2' are calculated using the Gaussian form of the thin lens equation (Meyer-Arendt, 1972). This equation states that the sum of the inverses of the object distance and the

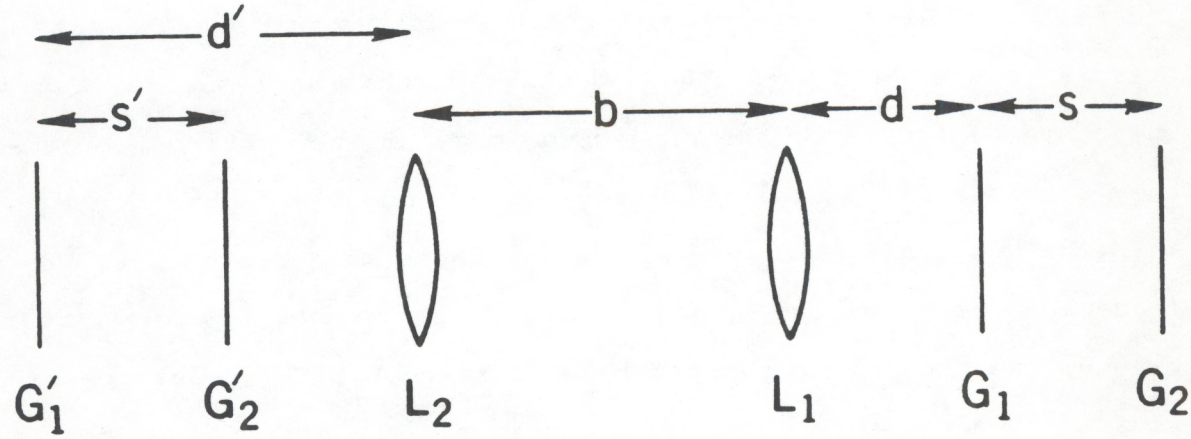

Fig. 3.3 Schematic diagram of telescope geometry showing telescope objective lens (L_2), real gratings (G_1 and G_2), and image gratings (G_1' and G_2').

image distance equals the inverse of the focal length. A diagram is shown in Fig. 3.4.

The subscript 1 refers to the image reflected by lens 1, and the subscript 2 refers to that reflected by lens 2.

For grating G_1 from Fig. 3.3, and from the definition $\frac{1}{o} + \frac{1}{i} = \frac{1}{f}$,

$$o_1 = d$$

$$\frac{1}{d} + \frac{1}{i_1} = \frac{1}{f_1} \qquad \Rightarrow \quad i_1 = \frac{f_1 d}{d - f_1}$$

$$o_2 = b - i_1 \qquad \Rightarrow \quad o_2 = \frac{bd - bf_1 - f_1 d}{d - f_1}$$

$$\frac{1}{i_2} = \frac{1}{f_2} - \frac{1}{o_2} \Rightarrow \quad i_2 = \frac{f_2 (bd - bf_1 - df_1)}{bd - bf_1 - df_1 - f_2 d + f_1 f_2}$$

$$d' = i_2 = \frac{f_2 (bd - bf_1 - df_1)}{bd - bf_1 - df_1 - f_2 d + f_1 f_2} \quad . \tag{3.9}$$

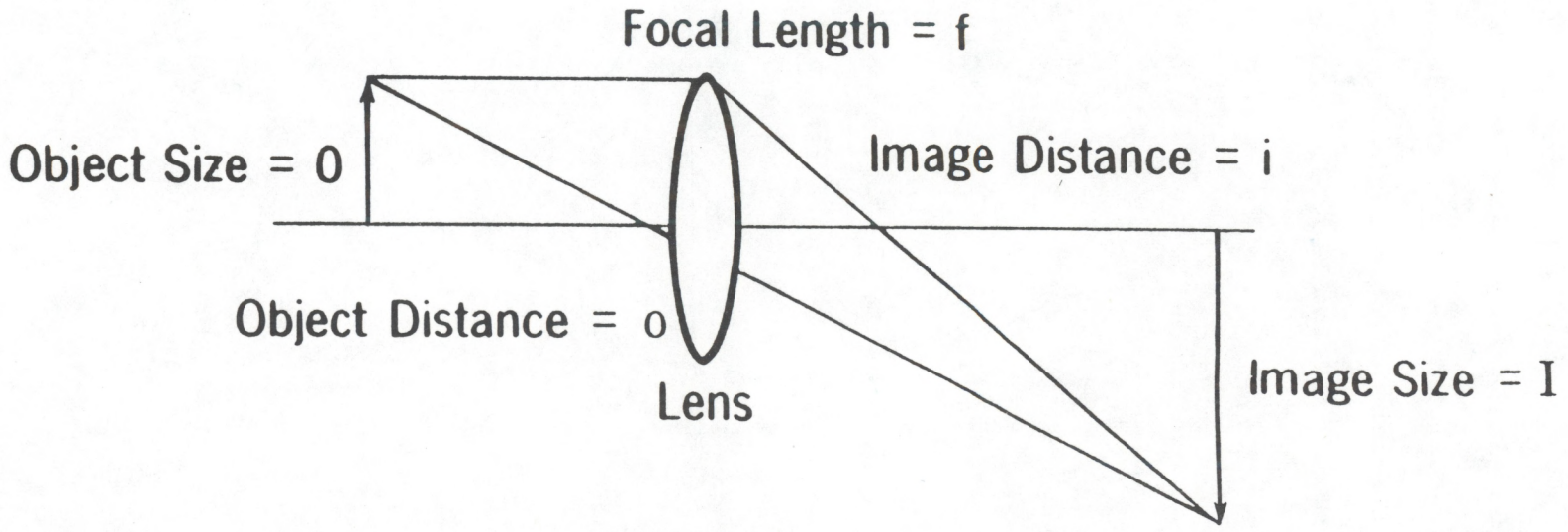

Fig. 3.4 Thin lens diagram

For grating G_2,

$$o_1 = d+s$$

$$\frac{1}{d+s} + \frac{1}{i_1} = \frac{1}{f_1} \qquad \Rightarrow \quad i_1 = \frac{f_1(d+s)}{d+s-f_1}$$

$$o_2 = b - i_1 \qquad \Rightarrow \quad o_2 = \frac{b(d+s-f_1) - f_1(d+s)}{d+s-f_1}$$

$$\frac{1}{i_2} = \frac{1}{f_2} - \frac{1}{o_2} \quad \Rightarrow \quad i_2 = \frac{f_2(bd+bs-bf_1-f_1d-f_1s)}{bd+bs-f_1b-f_1d-f_1s-f_2d-f_2s+f_2f_1}$$

$$s' = d' - i_2$$

$$s' = d' - \frac{f_2(bd+bs-bf_1-f_1d-f_1s)}{bd+bs-f_1b-f_1d-f_1s-f_2d-f_2s+f_2f_1} \quad . \tag{3.10}$$

To infer the grating wave numbers, we use the equation for transverse linear magnification, $M = i/o = I/O$. Therefore, for grating G_1,

$$o_1 = d$$

$$i_1 = \frac{f_1 d}{d-f_1}$$

$$\Rightarrow M_1 = \frac{f_1}{d-f_1}$$

$$o_2 = \frac{bd-bf_1-f_1d}{d-f_1}$$

$$i_2 = \frac{f_2(bd-bf_1-df_1)}{bd-bf_1-df_1-f_2d+f_1f_2}$$

$$\Rightarrow M_2 = M_1 \times \frac{i_2}{o_2} = \frac{f_1 f_2}{bd-bf_1-df_1-f_2d+f_1f_2}$$

$$K_1' = \frac{K_1(bd-bf_1-df_1-f_2d+f_1f_2)}{f_1f_2} \quad . \tag{3.11}$$

For grating G_2, following a similar analysis,

$$M_2 = \frac{f_1 f_2}{bd + bs - f_1 b - f_1 d - f_1 s - f_2 d - f_2 s + f_2 f_1} \quad .$$

Therefore,

$$K_2' = \frac{K_2 (bd + bs - f_1 b - f_1 d - f_1 s - f_2 d - f_2 s + f_2 f_1)}{f_1 f_2} \quad . \tag{3.12}$$

Where the telescope is focused at infinity, the new conditions establish b equal to $f_1 + f_2$ and d equal to f_1. In a similar manner, a new set of equations are obtained:

$$d' = f_2 \tag{3.13}$$

$$s' = M^2 s \tag{3.14}$$

$$K_1' = \frac{K_1}{M} \tag{3.15}$$

$$K_2' = \frac{K_2}{M} \quad , \tag{3.16}$$

where M is the telescope magnification, and is defined as $M = f_2/f_1$. In equations (3.15) and (3.16), the sign of the wave number has no significance.

3.6 Experiment

The experimental configuration shown in Fig. 3.5 was designed to verify the response of the system over a narrow section of the path. The transmitter consisted of an LED with a wavelength of 0.93 μm, a junction current of about 1 A, and 75 mW of estimated optical power. A Fresnel lens with a 40-cm focal length partially collimated the

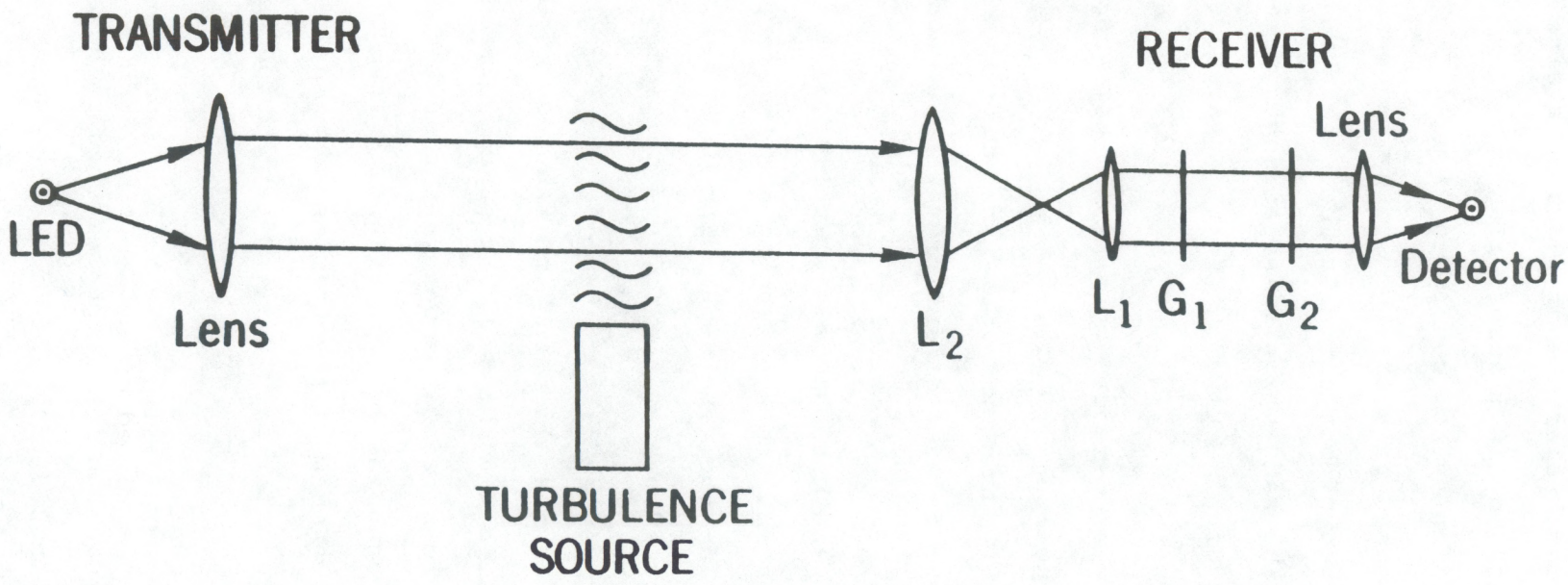

Fig. 3.5 Schematic diagram of experimental configuraiton showing transmitter, turbulence, and receiver geometry

light, with a square aperture of 27 cm on a side. The incoherent light was propagated 110 m across flat grassland to the receiver.

The turbulence source consisted of a 44 KW kerosene heater with a fan, and it was used to probe the system response. It generated a 23-cm diameter jet of hot air. It was separated 50 cm from the beam and located at the same height. The strength parameter C_N^2 observed had a minimum value of $3 \times 10^{-10}\ m^{-2/3}$, with an average turbulence velocity of 5.5 m/s.

The light was collected by a Kepler telescope at the receiver end of the path. The lens L_2 had a diameter of 22 cm and a focal length of 1 m, while L_1 had a diameter of 2.5 cm and a focal length of 10 cm. The telescope was focused at infinity with a magnification factor of 10. The grating G_1 had a grating constant of 11.00 lines/mm and G_2 of 10.30 lines/mm, and both had a diameter of 3 cm. Grating G_1 was located 10 cm behind the eyepiece of the telescope satisfy equations (4-13) through (4-16). The separation of G_2 was adjustable.

A lens located behind the filters collected the light onto a photodiode. This signal was amplified and fed into an analog-to-digital converter installed in a personal computer. This signal was also filtered with a 30 Hz to 1 KHz bandpass, and fed into a second analog input. To process the data, we calculated the power spectral density of the bandpass filtered signal. Then, it was normalized by the square of the mean of the unfiltered signal. And finally, the normalized spectra for each grating separation were averaged.

The results obtained from this experiment showed that the receiver responded to turbulent scales with a wavelength of 1.43 cm for the choice of gratings and telescope selected. The spectra was similar at frequencies below 300 Hz. Therefore, it was assumed that fluctuations

across the entire aperture were larger than the fluctuations of the spatially filtered component at these frequencies. Consequently, the response of the spatial filter was defined as the integral of the power spectrum above 300 Hz.

A linear relationship between the path position and the grating separation was noted. Therefore, the path-weighting function can be inferred by leaving the blower at a fixed position and varying the grating separation. The experiment also attempted to measure wind speed and turbulence strength in the natural atmosphere over a wide range of conditions. However, this objective was not achieved. These measurements should be possible with a more sensitive system.

The double spatial filtered receiver configuration was less efficient than the spatially filtered transmitter and receiver technique. It was not clear the reason for this loss of efficiency. However, there are techniques to improve its performance. The use of phase gratings instead of amplitude gratings should increase the scattering efficiency. For the analysis of velocity, covariance processing is recommended instead of the spectral analysis.

4. THE DIFFRACTION ANALYSIS

The diffraction analysis covers a complete study of an electromagnetic wave propagating through the atmosphere (Lee and Harp, 1969) and through the double-spatial filtering receiver in order to obtain the field intensity of the wave at the focal plane. A schematic diagram for this configuration is shown in Fig. 4.1. This configuration is composed of: (1) a layer of turbulence in the atmosphere, (2) two independent spatial filters located at ground level, (3) a thin

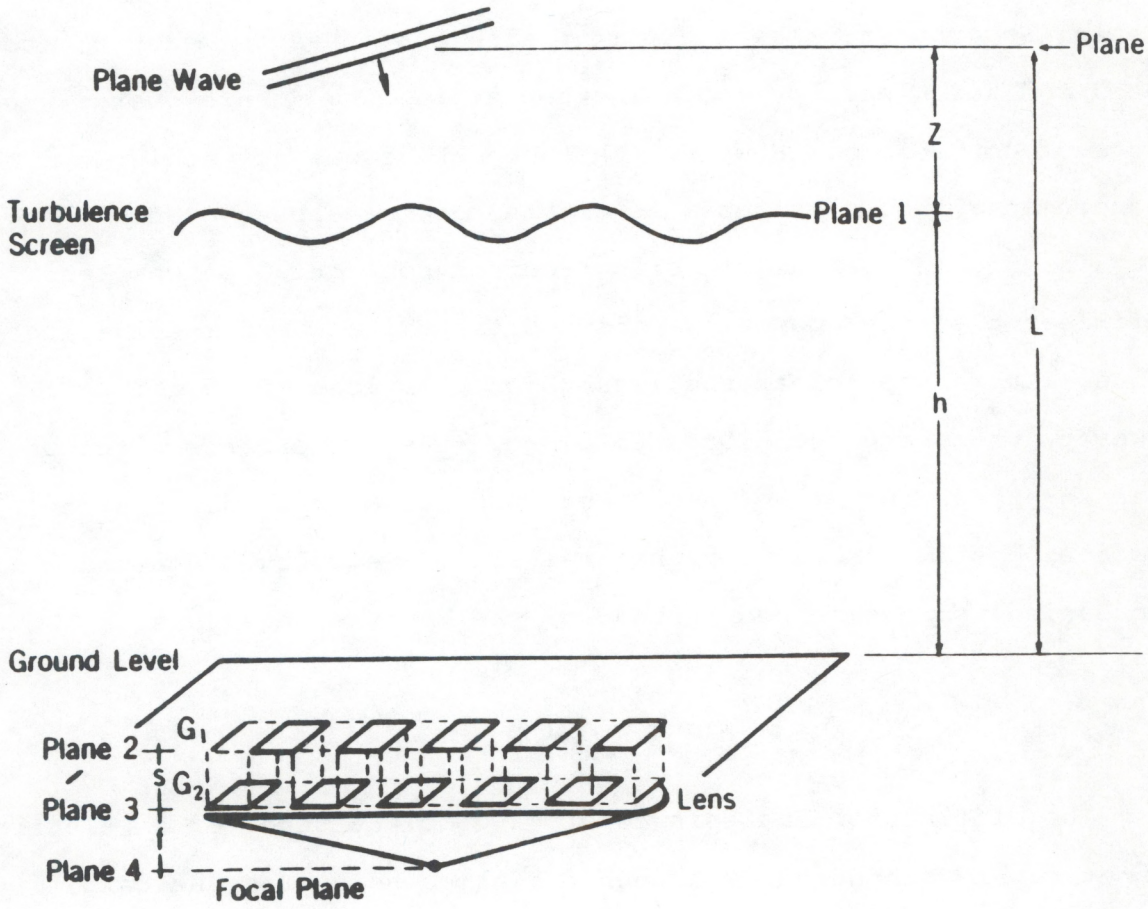

Fig. 4.1 Schematic diagram for the diffractional analysis showing the turbulence screen and the double-spatial filtering receiver.

lens to converge the signals to a common point, and (4) a focal plane where the field intensity is detected.

4.1 Propagation Through the Atmosphere

4.1.1 Propagation of a plane wave up to the slab of random refractivity

A plane wave propagating in the z direction with wave number k is incident upon an infinite slab. The slab contains a random refractivity which is Fourier analyzed into spatial frequency components. This first part of the analysis will be developed using the approximation of Huygens-Fresnel integral (Goodman, 1968).

For the analysis of a wave propagating in the z direction, the approximations made by the Huygens-Fresnel diffraction principle will be used to study the wave behavior through its path. This equation states that

$$U(x_0, y_0) = \frac{\exp(jkz)}{j\lambda z} \iint_{-\infty}^{\infty} U(x_1, y_1)$$

$$\times \exp\left\{ j\frac{k}{2z} \left[(x_0 - x_1)^2 + (y_0 - y_1)^2\right] \right\} dx_1 dy_1$$

where $U(x_0, y_0)$ represents the observed field strength, and $U(x_1, y_1)$ is the aperture field. Figure 4.2 shows a configuration for the diffraction geometry involved.

Thus, for the case of a plane wave,

$$U(x_0, y_0, 0) = \exp\{ j \vec{k}_\perp \cdot \vec{\rho}_0 \}$$

$$U(x_1, y_1, z) = \frac{e^{jkz}}{j\lambda z} \iint_{-\infty}^{\infty} U(x_0, y_0) \exp\{ j \frac{k}{2z} (\vec{\rho}_1 - \vec{\rho}_0)^2 \}$$

$$U(x_1, y_1, z_1) = \frac{\exp\{j k z_1\}}{j\lambda z_1} \int d^2 \vec{\rho}_0 \exp\{j \vec{k}_\perp \cdot \vec{\rho}_0\} \exp\left\{j \frac{k}{2z_1} \rho_1^2\right\}$$

$$\cdot \exp\left\{-j \frac{k}{z_1} \vec{\rho}_1 \cdot \vec{\rho}_0\right\} \exp\left\{j \frac{k}{2z_1} \rho_0^2\right\}$$

$$= \frac{\exp\{j k z_1\}}{j \lambda z_1} \exp\left\{j \frac{k}{2z_1} \rho_1^2\right\} \int d^2 \vec{\rho}_0 \exp\left\{j \frac{k}{2z_1} \rho_0^2\right\}$$

$$\cdot \exp\{j \vec{k}_\perp \cdot \vec{\rho}_0\} \exp\left\{-j \frac{k}{z_1} \vec{\rho}_1 \cdot \vec{\rho}_0\right\}$$

$$= \frac{\exp\{j k z_1\}}{j \lambda z_1} \exp\left\{j \frac{k}{2z_1} \rho_1^2\right\} \int d^2 \vec{\rho}_0$$

$$\cdot \exp\left\{j \frac{k}{2z_1} \rho_o^2\right\} \exp\left\{j \vec{\rho}_0 \cdot \left(\vec{k}_\perp - \frac{k}{z_1} \vec{\rho}_1\right)\right\} .$$

Using the identity

$$\int d^2x \exp\{j \alpha x\} \exp\{-\gamma x^2\} = \frac{\pi}{\gamma} \exp\left\{-\frac{\alpha^2}{4\gamma}\right\} ,$$

$$U(x_1, y_1, z_1) = \frac{\exp\{j k z_1\}}{j \lambda z_1} \exp\left\{j \frac{k}{2z_1} \rho_1^2\right\} j \frac{2z_1\pi}{k} \exp\left\{-j \frac{z_1}{2k} \left(\vec{k}_\perp - \frac{k}{z_1} \vec{\rho}_1\right)^2\right\}$$

$$= \exp\{j k z_1\} \exp\left\{j \frac{k}{2z_1} \rho_1^2\right\} \exp\left\{-j \frac{z_1}{2k} k_\perp^2 + j \vec{k}_\perp \vec{\rho}_1 - j \frac{k}{2z_1} \rho_1^2\right\}$$

$$= \exp\{j(\vec{k}_\perp \cdot \vec{\rho}_1 + k z_1)\} \exp\left\{-j \frac{z_1}{2k} k_\perp^2\right\} .$$

Figure 4.3 shows a schematic diagram of a plane wave propagating from z=0 to $z=z_1$. The wave number of the plane wave is decomposed into a transversal component and a component in the propagating direction z. The follow relationships are used to arrive at a complete solution at $z=z_1$.

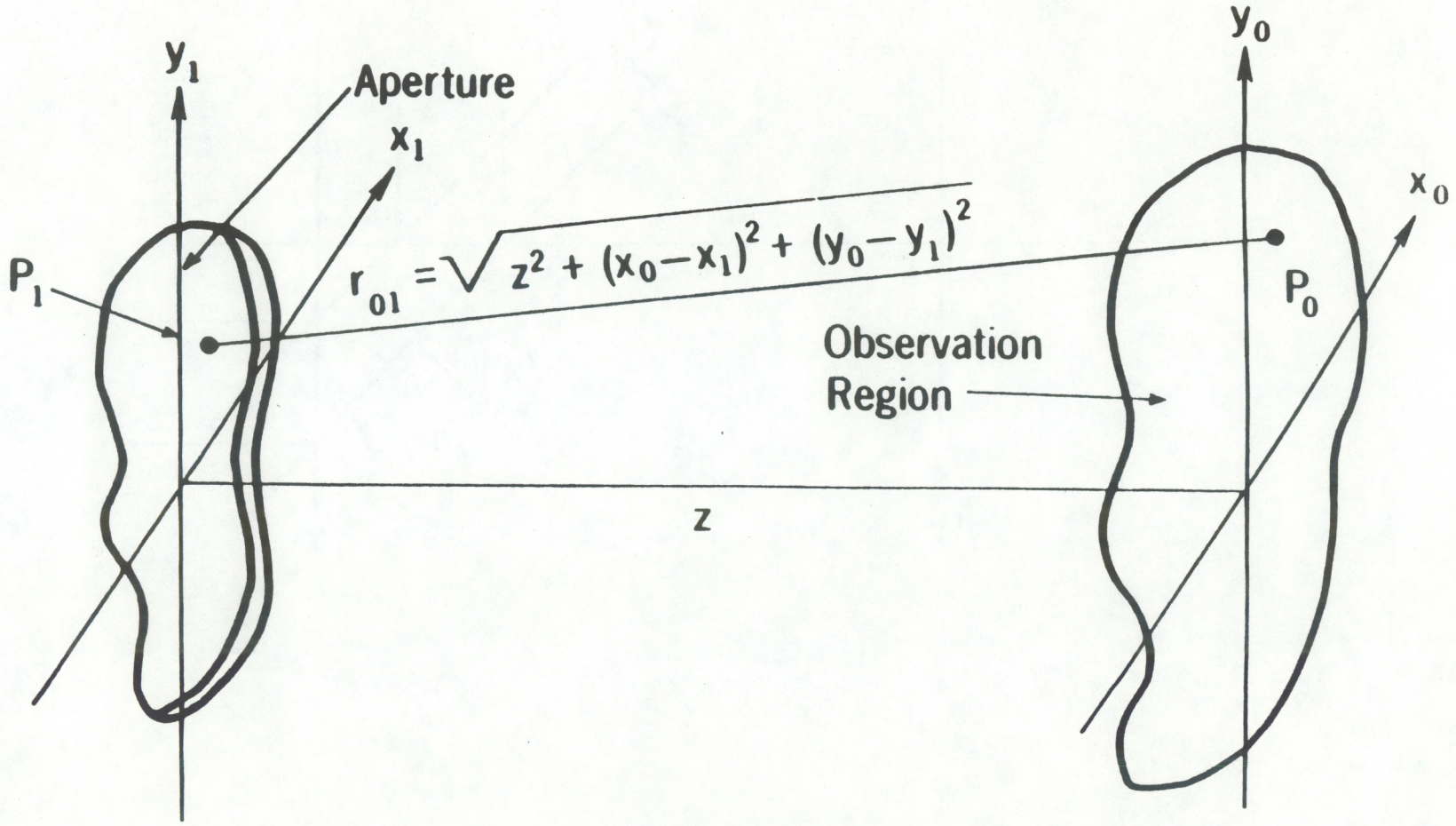

Fig. 4.2 Diffraction geometry

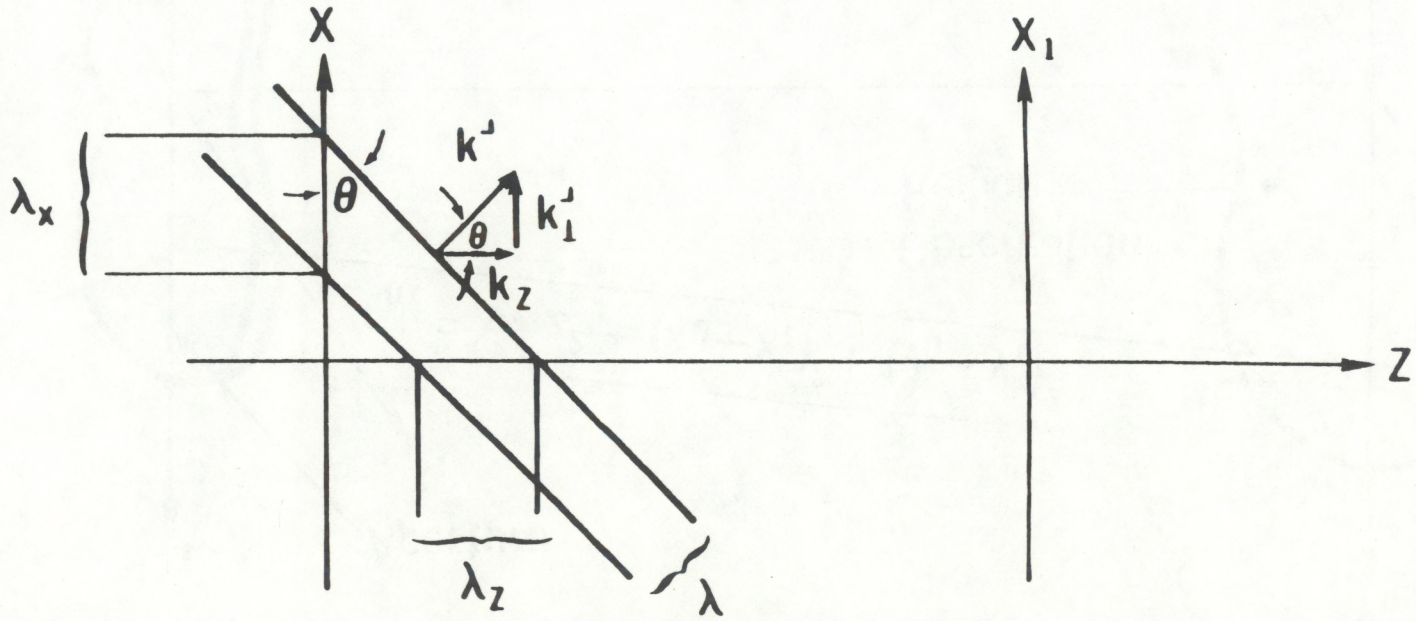

Fig. 4.3 Diagram for a plane wave propagating from $z = 0$ to $z = z_1$.

From the diagram it is observed that

$$\lambda_z = \frac{\lambda}{\cos\theta} \quad and \quad \lambda_x = \frac{\lambda}{\sin\theta} \quad .$$

Therefore,

$$\lambda_z = \frac{\lambda}{\sqrt{1 - (\lambda/\lambda_x)^2}} \quad ,$$

and using the definition $k = 2\pi/\lambda$,

$$k_z = k\sqrt{1 - (k_x - k)^2} = \sqrt{k^2 - k_x^2} \quad .$$

Generalizing,

$$k_z = \sqrt{k^2 - k_\perp^2}.$$

Applying these relations:

$$U(x, y, 0) = \exp\{j\vec{k}_\perp \cdot \vec{\rho}\}$$

$$U(x_1, y_1, z_1) = \exp\{j(\vec{k}_\perp \cdot \vec{\rho}_1 + \vec{k}_z z_1)\}$$

$$U(x_1, y_1, z_1) = \exp\left\{j\left(\vec{k}_\perp \cdot \vec{\rho}_1 + \sqrt{k^2 - k_\perp^2}\, z_1\right)\right\} \quad .$$

A comparison of the field wave obtained in the complete analysis from section b,

$$U(x_1, y_1, z_1) = \exp\left\{j\left(\vec{k}_\perp \cdot \vec{\rho}_1 + \sqrt{k^2 - k_\perp^2} z_1\right)\right\}$$

to that obtained from the Huygens-Fresnel integral approximation,

$$U(x_1, y_1, z_1) = \exp\{j(\vec{k}_\perp \cdot \vec{\rho}_1 + k z_1)\} \exp\left\{-j\left(\frac{z_1}{2k} k_\perp^2\right)\right\}$$

implies the following approximation:

$$\sqrt{k^2 - k_\perp^2}\, z_1 \approx \left[k - \frac{k_\perp^2}{2k}\right] z_1 .$$

Analyzing the left term:

$$\sqrt{k^2 - k_\perp^2}\, z_1 = k\sqrt{1 - \frac{k_\perp^2}{k^2}}\, z_1$$

and assuming that $|\vec{k}_\perp| << k$, then $\lambda << \lambda_x$. This condition is satisfied for very small values of θ. When θ gets close to 0°, the value of λ_x approaches infinity. On the other hand, as the angle θ gets larger, the value of λ_x approximates the value of λ. By using Taylor's series expansion, it shows the approximation implied in the Huygens-Fresnel integral equation:

$$k\sqrt{1 - \frac{k_\perp^2}{k^2} z_1} \approx k\left[1 - \frac{k_\perp^2}{2k^2}\right] z_1 = \left[k - \frac{k_\perp^2}{2k}\right] z_1 .$$

4.1.2 Effects of the slab of random refractivity on the plane wave

The slab of random refractivity imposes a phase perturbation on the wave, which is sinusoidal in ρ_1 and of peak magnitude $k\, a(\vec{K}_T)\, dz$:

$$\Delta\phi = k\, a(\vec{K}_T)\, dz \cos(\vec{K}_T \cdot \vec{\rho}_1 + b) ,$$

where b is the phase of the perturbation at the z-axis.

Upon exiting from the slab, the wave may be written as

$$U_T(x_1, y_1, z_1) = \exp\left\{ j\left(\vec{k}_\perp \cdot \vec{\rho}_1 + \sqrt{k^2 - k_\perp^2} z_1\right)\right\} \exp\{j\Delta\phi\} ,$$

and assuming $\Delta\phi << 2\pi$,

$$U_T(x_1, y_1, z_1) = \exp\left\{ j\left(\vec{k}_\perp \cdot \vec{\rho}_1 + \sqrt{k^2 - k_\perp^2} z_1\right)\right\}(1 + j\Delta\phi) .$$

The wave may be written as

$$U_T(x_1, y_1, z_1) = \exp\left\{ j \left(\vec{k}_\perp \cdot \vec{\rho}_1 + \sqrt{k^2 - k_\perp^2}\, z_1 \right) \right\}$$

$$\cdot [1 + j\, k\, a(\vec{K}_T)\, dz \cos(\vec{K}_T \cdot \vec{\rho}_1 + b)]$$

$$U_T(x_1, y_1, z_1) = \exp\left\{ j \left(\vec{k}_\perp \cdot \vec{\rho}_1 + \sqrt{k^2 - k_\perp^2} z_1 \right) \right\}$$

$$\cdot \left[1 + j k\, a(\vec{K}_T)\, dz \left(\frac{\exp\{ j\vec{K}_T \cdot \vec{\rho}_1 + b \} + \exp\{ -j(\vec{K}_T \cdot \vec{\rho}_1 + b) \}}{2} \right) \right]$$

$$U_T(x_1, y_1, z_1) = \exp\left\{ j \left(\vec{k}_\perp \cdot \vec{\rho}_1 + \sqrt{k^2 - k_\perp^2} z_1 \right) \right\}$$

$$+ j \frac{k\, a(\vec{K}_T)\, dz}{2} \exp\left\{ j \left(\vec{k}_\perp \cdot \vec{\rho}_1 + \sqrt{k^2 - k_\perp^2} z_1 \right) \right\} * \exp\{ j\vec{K}_T \cdot \vec{\rho}_1 + b \}$$

$$+ j \frac{k\, a(\vec{K}_T)\, dz}{2} \exp\left\{ j \left(\vec{k}_\perp \cdot \vec{\rho}_1 + \sqrt{k^2 - k_\perp^2} z_1 \right) \right\} \exp\{ -j(\vec{K}_T \cdot \vec{\rho}_1 + b) \} \quad .$$

For practical purposes, the resulting field will be represented as the summation of three component waves. The first term represents the original wave, and the other two terms represent the waves generated by the diffraction phenomenon. Thus,

$$U_T(x_1, y_1, z_1) = U_{T1} + U_{T2} + U_{T3} \quad .$$

4.1.3 Propagating the resulting waves up to the double-spatial filtering receiver

By using the analysis developed in Section 4.1.1, the resulting waves at the ground level entering the receiver may be written as

$$U_{T1}(x_2, y_2, L - z_1) = \exp\left\{ j \left(\vec{k}_\perp \cdot \vec{\rho}_2 + \sqrt{k^2 - k_\perp^2} z_1 \right) \right\} \exp\{ j\, k_{z1} (L - z_1) \} \, ,$$

where $k_{z1} = \sqrt{k^2 - k_\perp^2}$.

$$U_{T1}(x_2, y_2, L-z_1) = \exp\{j(\vec{k}_\perp \cdot \vec{\rho}_2)\} \exp\left\{j\sqrt{k^2 - k_\perp^2}\, L\right\}$$

$$U_{T2}(x_2, y_2, L-z_1) = j k \frac{a(\vec{k}_T)\, dz}{2}$$

$$\cdot \exp\left\{j\left(\vec{k}_\perp \cdot \vec{\rho}_2 + \sqrt{k^2 - k_\perp^2}\, z_1\right)\right\} \exp\{j \vec{k}_T \cdot \vec{\rho}_2 + b\} \exp\{j k_{z2}(L - z_1)\} \quad ,$$

where $k_{z2} = \sqrt{k^2 - (\vec{k}_\perp + \vec{k}_T)^2}$.

$$U_{T3}(x_2, y_2, L-z_1) = j\, k\, \frac{a(\vec{k}_T)\, dz}{2}$$

$$\cdot \exp\left\{j\left(\vec{k}_\perp \cdot \vec{\rho}_2 + \sqrt{k^2 - k_\perp^2}\, z_1\right)\right\}$$

$$\cdot \exp\{-j\,(\vec{k}_T \cdot \vec{\rho}_2 + b)\} \exp\{j k_{z3}(L - z_1)\} \quad ,$$

where $k_{z3} = \sqrt{k^2 - (\vec{k}_\perp - \vec{k}_T)^2}$.

4.2 Propagation of a Plane Wave through the Double-Spatial Filtering Receiver

To simplify the diffraction analysis over the whole path, we derive the effects of the spatial filter gratings and lens on a single plane wave. These results are then applied to the set of waves being received at the ground level to obtain the total field wave at the focal plane.

4.2.1 Effects of grating 1 on a plane wave

In this case the diffraction screen at the spatial filtering system is assumed to be caused by a sinusoidal amplitude grating defined by the transmittance function

$$t(\vec{\rho}) = \left[\frac{1}{2} + \frac{m}{2}\cos(\vec{K}_n \cdot \vec{\rho})\right] \quad ,$$

where m is the peak-to-peak change of amplitude transmittance across the screen. For this specific configuration, m is assumed to have a unitary value and K_n is the receiver wave number for the specific grating.

Therefore, at the receiver,

$$U(x_2, y_2, 0) = \exp\{j\vec{K}_{\perp G} \cdot \vec{\rho}_2\} \quad .$$

At grating 1,

$$U(x_2, y_2, 0) = \exp\{j\vec{K}_{\perp G} \cdot \vec{\rho}_2\} \left(\frac{1}{2} + \frac{\cos(\vec{K}_1 \cdot \vec{\rho}_2)}{2}\right)$$

$$= \exp\{j\vec{K}_{\perp G} \cdot \vec{\rho}_2\}$$

$$\cdot \left(\frac{1}{2} + \frac{1}{2}\left[\frac{\exp\{j\vec{K}_1 \cdot \vec{\rho}_2\} + \exp\{-j\vec{K}_1 \cdot \vec{\rho}_2\}}{2}\right]\right)$$

$$= \frac{\exp\{j\vec{K}_{\perp G} \cdot \vec{\rho}_2\}}{2} + \frac{1}{4}\exp\{j\vec{K}_{\perp G} \cdot \vec{\rho}_2\}\exp\{j\vec{K}_1 \cdot \vec{\rho}_2\}$$

$$+ \frac{1}{4}\exp\{j\vec{K}_{\perp G} \cdot \vec{\rho}_2\}\exp\{-j\vec{K}_1 \cdot \vec{\rho}_2\} \quad .$$

Propagating a distance s to grating 2,

$$U(x_3, y_3, s) = \frac{1}{2} \exp\{j\vec{K}_{\perp G} \cdot \vec{\rho}_3\} \exp\left\{j\sqrt{k_G^2 - k_{\perp G}^2}\, s\right\}$$

$$+ \frac{1}{4} \exp\{j\vec{K}_{\perp G} \cdot \vec{\rho}_3\} \exp\{j\vec{K}_1 \cdot \vec{\rho}_3\} \exp\left\{j\sqrt{k_G^2 - (\vec{K}_{\perp G} + \vec{K}_1)^2}\, s\right\}$$

$$+ \frac{1}{4} \exp\{j\vec{K}_{\perp G} \cdot \vec{\rho}_3\} \exp\{-j\vec{K}_1 \cdot \vec{\rho}_3\} \exp\left\{j\sqrt{k_G^2 - (\vec{K}_{\perp G} - \vec{K}_1)^2}\, s\right\} \quad .$$

At grating 2, assuming that $|\vec{K}_G| = |\vec{K}|$,

$$U(x_3, y_3, s) = [\frac{1}{2} \exp\{j \vec{K}_{\perp G} \cdot \vec{\rho}_3\} \exp\left\{j\sqrt{k^2 - k_{\perp G}^2}\, s\right\}$$

$$+ \frac{1}{4} \exp\{j \vec{\rho}_3 \cdot (\vec{K}_{\perp G} + \vec{K}_1)\} \exp\left\{j\sqrt{k^2 - (\vec{K}_{\perp G} + \vec{K}_1)^2}\, s\right\}$$

$$+ \frac{1}{4} \exp\{j \vec{\rho}_3 \cdot (\vec{K}_{\perp G} - \vec{K}_1)\} \exp\left\{j\sqrt{k^2 - (\vec{K}_{\perp G} - \vec{K}_1)^2}\, s\right\}]$$

$$\times \left[\frac{1}{2} + \frac{1}{4} \exp\{j \vec{K}_2 \cdot \vec{\rho}_3\} + \frac{1}{4} \exp\{-j \vec{K}_2 \cdot \vec{\rho}_3\}\right] .$$

$$U(x_3, y_3, s) = \frac{1}{4} \exp\{j \vec{K}_{\perp G} \cdot \vec{\rho}_3\} \exp\left\{j\sqrt{k^2 - k_{\perp G}^2}\, s\right\}$$

$$+ \frac{1}{8} \exp\{j \vec{\rho}_3 \cdot (\vec{K}_{\perp G} + \vec{K}_1)\} \exp\left\{j\sqrt{k^2 - (\vec{K}_{\perp G} + \vec{K}_1)^2}\, s\right\}$$

$$+ \frac{1}{8} \exp\{j \vec{\rho}_3 \cdot (\vec{K}_{\perp G} - \vec{K}_1)\} \exp\left\{j\sqrt{k^2 - (\vec{K}_{\perp G} - \vec{K}_1)^2}\, s\right\}$$

$$+ \frac{1}{8} \exp\{j \vec{\rho}_3 \cdot (\vec{K}_{\perp G} + \vec{K}_2)\} \exp\left\{j\sqrt{k^2 - k_{\perp G}^2}\, s\right\}$$

$$+ \frac{1}{16} \exp\{j \vec{\rho}_3 \cdot (\vec{K}_{\perp G} + \vec{K}_1 + \vec{K}_2)\} \exp\left\{j\sqrt{k^2 - (\vec{K}_{\perp G} + \vec{K}_1)^2}\, s\right\}$$

$$+ \frac{1}{16} \exp\{j \vec{\rho}_3 \cdot (\vec{K}_{\perp G} - \vec{K}_1 + \vec{K}_2)\} \exp\left\{j\sqrt{k^2 - (\vec{K}_{\perp G} - \vec{K}_1)^2}\, s\right\}$$

$$+ \frac{1}{8} \exp\{j \vec{\rho}_3 \cdot (\vec{K}_{\perp G} - \vec{K}_2)\} \exp\left\{j\sqrt{k^2 - k_{\perp G}^2}\, s\right\}$$

$$+ \frac{1}{16} \exp\{j \vec{\rho}_3 \cdot (\vec{K}_{\perp G} + \vec{K}_1 - \vec{K}_2)\} \exp\left\{j\sqrt{k^2 - (\vec{K}_{\perp G} + \vec{K}_1)^2}\, s\right\}$$

$$+ \frac{1}{16} \exp\{j \vec{\rho}_3 \cdot (\vec{K}_{\perp G} - \vec{K}_1 - \vec{K}_2)\} \exp\left\{j\sqrt{k^2 - (\vec{K}_{\perp G} - \vec{K}_1)}\, s\right\} .$$

4.2.2 Effect of the transfer function of the lens on the waves

The resulting wave field from the double spatial filtering system propagates through a converging lens of focal length f. The resulting amplitude distribution behind the lens is given by

$$U_{1'}(\vec{\rho}) = U_1(\vec{\rho})\ P(\vec{\rho})\ \exp\left\{-j\frac{k}{2f}(\rho^2)\right\},$$

where $U_{1'}(\vec{\rho})$ is the amplitude distribution placed inmediately in front of the converging lens; $P(\vec{\rho})$ is a pupil function which determine the finite extent of the lens aperture. For the specific configuration of this analysis, a Gaussian function described by

$$P(\vec{\rho}) = e^{-\alpha\rho^2}$$

was chosen. The grating structure is bounded by the Gaussian aperture with $\alpha = 2/D^2$, where D represents the aperture size, and α was calculated for a value of 1/e, the intensity diameter, and

$$\exp\left(-j\frac{k}{2f}\ \rho^2\right)$$

represents the quadratic phase shift.

Therefore, at the lens,

$$U_L(x_3, y_3, s) = U(x_3, y_3, s)\ \exp\left\{-\frac{2}{D^2}\ \rho_3^2\right\}\ \exp\left\{-j\frac{k}{2f}\ \rho_3^2\right\}\ .$$

To propagate the waves a distance f to the focal plane, using the approximation of the Huygens-Fresnel integral,

$$U(x_4, y_4, f) = \frac{\exp\{jkf\}}{j\lambda f}\int d^2\ \vec{\rho}_3\ \ U_L(x_3, y_3, s)\ \exp\left\{j\frac{k}{2f}(\vec{\rho}_4 - \vec{\rho}_3)^2\right\}$$

$$U(x_4, y_4, f) = \frac{\exp\{jkf\}}{j\lambda f}\ \exp\left\{j\frac{k}{2f}\ \rho_4^2\right\}\int d^2\ \vec{\rho}_3\ \ U_L(x_3, y_3, s)$$

$$\cdot\ \exp\left\{j\frac{k}{2f}\ \rho_3^2\right\}\ \exp\left\{-j\frac{k}{f}\ \vec{\rho}_3 \cdot \vec{\rho}_4\right\}\ .$$

4.3 Field Wave Detected at the Focal Plane

The total field wave detected at the focal plane is obtained by applying the general form calculated in Section 4.2, to the three specific wave cases calculated in Section 4.1. For practical purposes, the total field wave remains the summation of the three wave fields U_1, U_2, and U_3.

And, after some manipulation of terms, the general case for a wave at the focal plane is given by

$$
\begin{aligned}
U(x_4, y_4, f) = & \frac{\exp\{jkf\}}{j\lambda f} \exp\left\{ j\frac{k}{2f}\rho_4^2 \right\} \frac{D^2\pi}{2} \\
& \times \quad \frac{1}{4} \exp\left\{ j\sqrt{k^2 - k_{\perp G}^2}\, s \right\} \exp\left\{ -\frac{D^2}{8} \left(\vec{K}_{\perp G} - \frac{k}{f} \vec{\rho}_4 \right)^2 \right\} \\
& + \frac{1}{8} \exp\left\{ j\sqrt{k^2 - (\vec{K}_{\perp G} + \vec{K}_1)^2}\, s \right\} \exp\left\{ -\frac{D^2}{8} \left(\vec{K}_{\perp G} + \vec{K}_1 - \frac{k}{f} \vec{\rho}_4 \right)^2 \right\} \\
& + \frac{1}{8} \exp\left\{ j\sqrt{k^2 - (\vec{K}_{\perp G} - \vec{K}_1)^2}\, s \right\} \exp\left\{ -\frac{D^2}{8} \left(\vec{K}_{\perp G} - \vec{K}_1 - \frac{k}{f} \vec{\rho}_4 \right)^2 \right\} \\
& + \frac{1}{8} \exp\left\{ j\sqrt{k^2 - k_{\perp G}^2}\, s \right\} \exp\left\{ -\frac{D^2}{8} \left(\vec{K}_{\perp G} + \vec{K}_2 - \frac{k}{f} \vec{\rho}_4 \right)^2 \right\} \\
& + \frac{1}{16} \exp\left\{ j\sqrt{k^2 - (\vec{K}_{\perp G} + \vec{K}_1)^2}\, s \right\} \exp\left\{ -\frac{D^2}{8} \left(\vec{K}_{\perp G} + \vec{K}_1 + \vec{K}_2 - \frac{k}{f} \vec{\rho}_4 \right)^2 \right\} \\
& + \frac{1}{16} \exp\left\{ j\sqrt{k^2 - (\vec{K}_{\perp G} - \vec{K}_1)^2}\, s \right\} \exp\left\{ -\frac{D^2}{8} \left(\vec{K}_{\perp G} - \vec{K}_1 + \vec{K}_2 - \frac{k}{f} \vec{\rho}_4 \right)^2 \right\} \\
& + \frac{1}{8} \exp\left\{ j\sqrt{k^2 - k_{\perp G}^2}\, s \right\} \exp\left\{ -\frac{D^2}{8} \left(\vec{K}_{\perp G} - \vec{K}_2 - \frac{k}{f} \vec{\rho}_4 \right)^2 \right\} \\
& + \frac{1}{16} \exp\left\{ j\sqrt{k^2 - (\vec{K}_{\perp G} + \vec{K}_1)^2}\, s \right\} \exp\left\{ -\frac{D^2}{8} \left(\vec{K}_{\perp G} + \vec{K}_1 - \vec{K}_2 - \frac{k}{f} \vec{\rho}_4 \right)^2 \right\} \\
& + \frac{1}{16} \exp\left\{ j\sqrt{k^2 - (\vec{K}_{\perp G} - \vec{K}_1)^2}\, s \right\} \exp\left\{ -\frac{D^2}{8} \left(\vec{K}_{\perp G} - \vec{K}_1 - \vec{K}_2 - \frac{k}{2f} \vec{\rho}_4 \right)^2 \frac{D^2}{8} \right\} .
\end{aligned}
$$

Thus, there are three waves entering the receiver:

$$U_1(x_2, y_2, L) = \exp\{j\,\vec{k}_\perp \cdot \vec{\rho}_2\} \exp\left\{j\sqrt{k^2 - k_\perp^2}\; L\right\}$$

$$U_2(x_2, y_2, L) = j\,k\frac{a(\vec{K}_T)\,dz}{2} \exp\left\{j\left(\vec{k}_\perp \cdot \vec{\rho}_2 + \sqrt{k^2 - k_\perp^2}\; z\right)\right\}$$

$$\cdot \exp\{j(\vec{K}_T \cdot \vec{\rho}_2 + b)\} \exp\left\{j\sqrt{k^2 - (\vec{k}_\perp + \vec{K}_T)^2}\,(L-Z)\right\}$$

$$U_3(x_2, y_2, L) = j\,k\,\frac{a(\vec{K}_T)\,dz}{2} \exp\left\{j\left(\vec{k}_\perp \cdot \vec{\rho}_2 + \sqrt{k^2 - k_\perp^2}\; z\right)\right\}$$

$$\cdot \exp\{-j(\vec{K}_T \cdot \vec{\rho}_2 + b)\} \exp\left\{j\sqrt{k^2 - (\vec{k}_\perp - \vec{K}_T)^2}\,(L-Z)\right\} \quad .$$

Considering plane 2 as the new reference, the waves may be written as

$$U_1(x_2, y_2, 0) = \exp\{j(\vec{k}_\perp \cdot \vec{\rho}_2)\} \exp\left\{j\sqrt{k^2 - k_\perp^2}\; L\right\} \quad ; \quad \vec{k}_\perp = \vec{k}_{\perp G}$$

$$U_2(x_2, y_2, 0) = j\,k\,\frac{a(\vec{K}_T)\,dz}{2}\, e^{jb} \exp\{j\,\vec{\rho}_2 \cdot (\vec{k}_\perp + \vec{K}_T)\}$$

$$\cdot \exp\left\{jz\left(\sqrt{k^2 - k_\perp^2} - \sqrt{k^2 - (\vec{k}_\perp + \vec{K}_T)^2}\right)\right\}$$

$$\cdot \exp\left\{jL\sqrt{k^2 - (\vec{k} + \vec{K}_T)^2}\right\} \; ; \quad \vec{k}_{\perp G} = \vec{k}_\perp + \vec{K}_T$$

$$U_3(x_2, y_2, 0) = j\,k\,\frac{a(\vec{K}_T)\,dz}{2}\, e^{-jb} \exp\{j\,\vec{\rho}_2 \cdot (\vec{k}_\perp - \vec{K}_T)\}$$

$$\cdot \exp\left\{jz\left(\sqrt{k^2 - k_\perp^2} - \sqrt{k^2 - (\vec{k}_\perp - \vec{K}_T)^2}\right)\right\}$$

$$\cdot \exp\left\{jL\sqrt{k^2 - (\vec{k}_\perp - \vec{K}_T)^2}\right\} \; ; \quad \vec{k}_{\perp G} = \vec{k}_\perp - \vec{K}_T \quad .$$

The resulting wave field at the focal plane is given by the following 27 terms.

$$U = \frac{\mathrm{D}^2 e^{fik+\frac{ikp^2}{2f}+Li\sqrt{k^2-{k_t}^2}}k}{64fi}$$

$$\times \left[\; 2e^{is\sqrt{k^2-(-K_1+k_t)^2}-\frac{\mathrm{D}^2\left(-\frac{kp}{f}-K_1+k_t\right)^2}{8}}\right.$$

$$+ e^{is\sqrt{k^2-(-K_1+k_t)^2}-\frac{\mathrm{D}^2\left(-\frac{kp}{f}-K_1-K_2+k_t\right)^2}{8}}$$

$$+ e^{is\sqrt{k^2-(-K_1+k_t)^2}-\frac{\mathrm{D}^2\left(-\frac{kp}{f}-K_1+K_2+k_t\right)^2}{8}}$$

$$+ 2e^{is\sqrt{k^2-(K_1+k_t)^2}-\frac{\mathrm{D}^2\left(-\frac{kp}{f}+K_1+k_t\right)^2}{8}}$$

$$+ e^{is\sqrt{k^2-(K_1+k_t)^2}-\frac{\mathrm{D}^2\left(-\frac{kp}{f}+K_1-K_2+k_t\right)^2}{8}}$$

$$\left. + e^{is\sqrt{k^2-(K_1+k_t)^2}-\frac{\mathrm{D}^2\left(-\frac{kp}{f}+K_1+K_2+k_t\right)^2}{8}}\right.$$

$$+ 4e^{is\sqrt{k^2-{k_t}^2}-\frac{D^2\left(-\frac{kp}{f}+k_t\right)^2}{8}}$$

$$+ 2e^{is\sqrt{k^2-{k_t}^2}-\frac{D^2\left(-\frac{kp}{f}-K_2+k_t\right)^2}{8}}$$

$$+ 2e^{is\sqrt{k^2-{k_t}^2}-\frac{D^2\left(-\frac{kp}{f}+K_2+k_t\right)^2}{8}} \Bigg]$$

$$+ \frac{D^2 e^{i\left(kf+\frac{kp^2}{2f}+L\sqrt{k^2-(K_T+k_T)^2}\right)} dzkk_0 a(K_T)}{128f}$$

$$\times \Bigg[2e^{is\sqrt{k^2-(-K_1+k_t)^2}-\frac{D^2\left(-\frac{kp}{f}-K_1+K_T+k_T\right)^2}{8}}$$

$$+ e^{is\sqrt{k^2-(-K_1+k_t)^2}-\frac{D^2\left(k2-\frac{kp}{f}-K_1+K_T+k_T\right)^2}{8}}$$

$$+ e^{is\sqrt{k^2-(-K_1+k_t)^2}-\frac{D^2\left(-\frac{kp}{f}-K_1-K_2+K_T+k_T\right)^2}{8}}$$

$$+ 2e^{is\sqrt{k^2-(K_1+k_t)^2}} - \frac{D^2\left(-\frac{kp}{f}+K_1+K_T+k_T\right)^2}{8}$$

$$+ e^{is\sqrt{k^2-(K_1+k_t)^2}} - \frac{D^2\left(-\frac{kp}{f}+K_1-K_2+K_T+k_T\right)^2}{8}$$

$$+ e^{is\sqrt{k^2-(K_1+k_t)^2}} - \frac{D^2\left(-\frac{kp}{f}+K_1+K_2+K_T+k_T\right)^2}{8}$$

$$+ 4e^{is\sqrt{k^2-k_t^2}} - \frac{D^2\left(-\frac{kp}{f}+K_T+k_T\right)^2}{8}$$

$$+ 2e^{is\sqrt{k^2-k_t^2}} - \frac{D^2\left(-\frac{kp}{f}-K_2+K_T+k_T\right)^2}{8}$$

$$+ 2e^{is\sqrt{k^2-k_t^2}} - \frac{D^2\left(-\frac{kp}{f}+K_2+K_T+k_T\right)^2}{8} \Bigg]$$

$$+ \frac{D^2 e^{i\left(kf+\frac{kp^2}{2f}+L\sqrt{k^2-(K_T+k_T)^2}\right)} dzkk_0 a(K_T)}{128f}$$

$$\times \left[2e^{is\sqrt{k^2-(-K_1+k_t)^2}} - \frac{D^2\left(-\frac{kp}{f}-K_1-K_T+k_T\right)^2}{8} \right.$$

$$+ e^{is\sqrt{k^2-(-K_1+k_t)^2}} - \frac{D^2\left(k2-\frac{kp}{f}-K_1-K_T+k_T\right)^2}{8}$$

$$+ e^{is\sqrt{k^2-(-K_1+k_t)^2}} - \frac{D^2\left(-\frac{kp}{f}-K_1-K_2-K_T+k_T\right)^2}{8}$$

$$+ 2e^{is\sqrt{k^2-(K_1+k_t)^2}} - \frac{D^2\left(-\frac{kp}{f}+K_1-K_T+k_T\right)^2}{8}$$

$$+ e^{is\sqrt{k^2-(K_1+k_t)^2}} - \frac{D^2\left(-\frac{kp}{f}+K_1-K_2-K_T+k_T\right)^2}{8}$$

$$+ e^{is\sqrt{k^2-(K_1+k_t)^2}} - \frac{D^2\left(-\frac{kp}{f}+K_1+K_2-K_T+k_T\right)^2}{8}$$

$$+ 4e^{is\sqrt{k^2-k_t{}^2}} - \frac{D^2\left(-\frac{kp}{f}-K_T+k_T\right)^2}{8}$$

$$+ 2e^{is\sqrt{k^2-k_t{}^2}} - \frac{D^2\left(-\frac{kp}{f} - K_2 - K_T + k_T\right)^2}{8}$$

$$+ 2e^{is\sqrt{k^2-k_t{}^2}} - \frac{D^2\left(-\frac{kp}{f} + K_2 - K_T + k_T\right)^2}{8} \Bigg]$$

The peak locations explain the scattering history and can be used to select terms that are interesting. They are given by the following.

Due to U_1 :

1. $\vec{\rho}_4 = \frac{f}{k}\vec{K}_\perp$

2. $\vec{\rho}_4 = \frac{f}{k}(\vec{K}_\perp + \vec{K}_1)$

3. $\vec{\rho}_4 = \frac{f}{k}(\vec{K}_\perp - \vec{K}_1)$

4. $\vec{\rho}_4 = \frac{f}{k}(\vec{K}_\perp + \vec{K}_2)$

5. $\vec{\rho}_4 = \frac{f}{k}(\vec{K}_\perp + \vec{K}_1 + \vec{K}_2)$

6. $\vec{\rho}_4 = \frac{f}{k}(\vec{K}_\perp - \vec{K}_1 + \vec{K}_2)$

7. $\vec{\rho}_4 = \frac{f}{k}(\vec{K}_\perp - \vec{K}_2)$

8. $\vec{\rho}_4 = \frac{f}{k}(\vec{K}_\perp + \vec{K}_1 - \vec{K}_2)$

9. $\vec{\rho}_4 = \frac{f}{k}(\vec{K}_\perp - \vec{K}_1 - \vec{K}_2)$

Due to U_2:

10. $\vec{\rho}_4 = \frac{f}{k}(\vec{K}_\perp + \vec{K}_T)$

11. $\vec{\rho}_4 = \frac{f}{k}(\vec{K}_\perp + \vec{K}_T + \vec{K}_1)$

12. $\vec{\rho}_4 = \frac{f}{k}(\vec{K}_\perp + \vec{K}_T - \vec{K}_1)$

13. $\vec{\rho}_4 = \frac{f}{k}(\vec{K}_\perp + \vec{K}_T + \vec{K}_2)$

14. $\vec{\rho}_4 = \frac{f}{k}(\vec{K}_\perp + \vec{K}_T + \vec{K}_1 + \vec{K}_2)$

15. $\vec{\rho}_4 = \frac{f}{k}(\vec{K}_\perp + \vec{K}_T - \vec{K}_1 + \vec{K}_2)$

16. $\vec{\rho}_4 = \frac{f}{k}(\vec{K}_\perp + \vec{K}_T - \vec{K}_2)$

17. $\vec{\rho}_4 = \frac{f}{k}(\vec{K}_\perp + \vec{K}_T + \vec{K}_1 - \vec{K}_2)$

18. $\vec{\rho}_4 = \frac{f}{k}(\vec{K}_\perp + \vec{K}_T - \vec{K}_1 - \vec{K}_2)$

Due to U_3:

19. $\vec{\rho}_4 = \frac{f}{k}(\vec{K}_\perp - \vec{K}_T)$

20. $\vec{\rho}_4 = \frac{f}{k}(\vec{K}_\perp - \vec{K}_T + \vec{K}_1)$

21. $\vec{\rho}_4 = \frac{f}{k}(\vec{K}_\perp - \vec{K}_T - \vec{K}_1)$

22. $\vec{\rho}_4 = \frac{f}{k}(\vec{K}_\perp - \vec{K}_T + \vec{K}_2)$

23. $\vec{\rho}_4 = \frac{f}{k}(\vec{K}_\perp - \vec{K}_T + \vec{K}_1 + \vec{K}_2)$

24. $\vec{\rho}_4 = \frac{f}{k}(\vec{K}_\perp - \vec{K}_T + \vec{K}_2)$

25. $\vec{\rho}_4 = \frac{f}{k}(\vec{K}_\perp - \vec{K}_T - \vec{K}_2)$

26. $\vec{\rho}_4 = \frac{f}{k}(\vec{K}_\perp - \vec{K}_T + \vec{K}_1 - \vec{K}_2)$

27. $\vec{\rho}_4 = \frac{f}{k}(\vec{K}_\perp - \vec{K}_T - \vec{K}_1 - \vec{K}_2)$

5. CONCLUSIONS

The studies of wave propagation in a turbulent medium have a direct relevance in the communications field. The design of reliable space and terrestrial high data rate communications systems require estimates of the temporal bandwidth limitations imposed by the random atmosphere. It produces fluctuations in the wave amplitude and phase as observed at a remote point. The impact of these fluctuations on a new optical remote sensing technique using a double-spatial filtering receiver has been presented.

The spatial filtering techniques proposed that the turbulence intensity and spectral shape could be profiled by observing the variance of the signal for different wavelength spatial filters. Also, the wind velocity could be profiled from the frequency contents of the signal under the same circumstances. The refractive-index fluctuations are decomposed at each path position into their transverse two-dimensional spatial Fourier component. As a result, the full scintillation pattern is the superposition of the diffraction patterns produced by all Fourier components of the refractive index at each path position.

A previously developed geometrical analysis for the double-spatial filtering technique was presented in Section 3. But the implementation of the system did not provide the expected results. Therefore, the objective of this research was to present a complete analysis of an electromagnetic wave propagating through the atmosphere and through a double-spatial filtering receiver. This study has been achieved in the previous chapter on the diffraction analysis. The wave field calculated at the focal plane consists of a total of 27 terms. Physically, further research should explore the contribution of each of these terms.

The physical quantity of interest is represented by the intensity of the field wave at the detector. The intensity of the field wave has a real value. This parameter is proportional to the levels of voltage that could be observed if a detector is placed at the focal plane to capture the signal. The intensity of the field wave was calculated by multiplying the 27 terms at the focal plane by their complex conjugate, obtaining 729 terms.

Three groups of terms were identified. The first group was independent of the random refractivity field of turbulence. A second group showed a linear dependency, and a third group showed a quadratic dependency on the random refractivity field of turbulence. By assuming very small values of the turbulence field, the third group was neglected. Thus, the intensity of the field wave was reduced to 405 complex terms. After some manipulation, 207 real terms were finally established.

The previous chapter listed the location of the 27 peaks detected at the focal plane. This last analysis aimed to select one term of the 207 terms to extend the research for understanding the range of

frequencies feasible in this study. Modeling the sun requires a partially coherent source. This is accomplished by integrating over a distribution of incident angles with a Gaussian distribution.

The term that was selected combines the following peak locations:

$$1. \quad \vec{\rho}_4 = \frac{f}{k}\vec{K}_\perp \ , \quad \textit{and}$$

$$15. \quad \vec{\rho}_4 = \frac{f}{K}(\vec{k}_\perp + \vec{K}_T - \vec{K}_1 + \vec{K}_2) \ .$$

The complete expression for this term is

$$t_{59} = \frac{1}{j8}\left(\frac{D^2\pi}{\lambda f}\right)^2 \vec{k}\, a(\vec{K}_T)\, dz(2/64)$$

$$\cdot \cos\left[L\left(\frac{K_T^2 + 2\vec{k}_\perp\vec{K}_T}{2k}\right) - z\left(\frac{K_T^2 + 2\vec{k}_\perp\vec{K}_T}{2k}\right) - b + s\left(\frac{K_1^2 - 2\vec{k}_\perp\vec{K}_1}{2k}\right)\right]$$

$$\cdot \exp\left\{-\frac{D^2}{8}\left[\left(\vec{K}_\perp - \frac{k}{f}\vec{\rho}_4\right)^2 + \left(\vec{K}_\perp + \vec{K}_T - \vec{K}_1 + \vec{K}_2 - \frac{k}{f}\vec{\rho}_4\right)^2\right]\right\} \ .$$

The path resolution is found from

$$i(\vec{k}_\perp) = \int_{-\infty}^{\infty} d\vec{K}_\perp \, I(\vec{K}_\perp) \, \frac{1}{\sqrt{2\pi}\,\sigma_R} \exp\left\{-\frac{k_\perp^2}{2\sigma_R^2}\right\} ,$$

where

$$\frac{\sigma_R}{k_z} \approx \frac{D_s}{2\,z_s}$$

σ_R represents the standard deviation of the wavenumber transverse component,

$\vec{k}_z$ is the component of the wavenumber in the propagation direction,

D_s is the diameter of the source, and

z_s is the distance to the source from the scattering plane.

Thus,

$$C = \frac{1}{j512}\left(\frac{D^2\pi}{\lambda f}\right)^2 \vec{k}\, a(\vec{K}_T)\, dz \cdot \frac{1}{\sqrt{2\pi}\sigma_R}$$

$$i(\vec{k}_\perp) = C \int_{-\infty}^{\infty} d\vec{k}_\perp \exp\left\{-\frac{D^2}{8}\left[\left(\vec{k}_\perp - \frac{k}{f}\vec{\rho}_4\right)^2 + \left(\vec{k}_\perp + \vec{K}_T - \vec{K}_1 + \vec{K}_2 - \frac{k}{f}\vec{\rho}_4\right)^2\right]\right\}$$

$$\cdot \exp\left\{-jL\left(\frac{K_T^2 + 2\vec{k}_\perp\vec{K}_T}{2k}\right)\right\} \exp\left\{+jz\left(\frac{K_T^2 + 2\vec{k}_\perp\vec{K}_T}{2k}\right)\right\}$$

$$\cdot e\{jb\} \exp\left\{-js\left(\frac{K_1^2 - 2\vec{k}_\perp\vec{K}_1}{2k}\right)\right\} * \exp\left\{-k_\perp^2\left(\frac{1}{2\sigma_R^2}\right)\right\} .$$

The path resolution for this specific term is found from

$$i(\vec{k}_\perp) = \frac{1}{j512}\left(\frac{D^2\pi}{\lambda f}\right)^2 \vec{k}\, a(\vec{K}_T)\, dz \frac{1}{\sqrt{2\pi}\,\sigma_R}$$

$$\cdot \exp\left\{-\frac{D^2}{8}\left[(\vec{K}_T - \vec{K}_1 + \vec{K}_2)^2 - 2\frac{k}{f}\vec{\rho}_4(\vec{K}_T - \vec{K}_1 + \vec{K}_2) + 2\frac{k^2}{f^2}\rho_4^2\right]\right\}$$

$$\cdot \exp\left\{-j\frac{K_T^2}{2k}h\right\} \exp\{jb\} \exp\left\{-js\frac{K_1^2}{2k}\right\}$$

$$\cdot \sqrt{\frac{\pi}{\frac{D^2}{4} + \frac{1}{2\sigma_R^2}}}$$

$$\cdot \exp\left\{\frac{\left[\frac{D^2}{2}\frac{k}{f}\vec{\rho}_4 - \frac{D^2}{4}(\vec{K}_T - \vec{K}_1 + \vec{K}_2) - j\frac{\vec{K}_T}{k}h + js\frac{\vec{K}_1}{k}\right]^2}{D^2 + \frac{2}{\sigma_R^2}}\right\} .$$

A detector is placed at the focal plane to receive the different spots. The integral of the intensity over the whole detector is

$$i(\vec{\rho}_4) = \int_{-\infty}^{\infty} d^2\vec{\rho}_4\, I(\vec{\rho}_4) ,$$

which is proportional to a photodetector output signal.

If

$$c = \frac{1}{j512}\left(\frac{D^2\pi}{\lambda f}\right)^2 \vec{k}\, a(\vec{K}_T)\, dz\, \frac{1}{\sqrt{2\pi}\sigma_R}\sqrt{\frac{\pi}{\frac{D^2}{4}+\frac{1}{2\sigma_R^2}}}\ ,$$

$$I(\vec{\rho}_4) = c\int_{-\infty}^{+\infty} d\rho_4^2 \exp\left\{-\frac{D^2}{8}\left[(\vec{K}_T-\vec{K}_1+\vec{K}_2)^2 - 2\frac{k}{f}\vec{\rho}_4(\vec{K}_T-\vec{K}_1+\vec{K}_2) + 2\frac{k^2}{f^2}\rho_4^2\right]\right\}$$

$$\cdot \exp\left\{-j\left[\frac{K_T^2}{2k}h - b + s\frac{K_1^2}{2k}\right]\right\}$$

$$\cdot \exp\left\{\frac{\left(\frac{D^2}{2}\frac{k}{f}\vec{\rho}_4\right)^2 + D^2\frac{k}{f}\vec{\rho}_4\left[j\left(\frac{s\vec{K}_1}{k}-\frac{\vec{K}_T h}{k}\right)-\frac{D^2}{4}(\vec{K}_T-\vec{K}_1+\vec{K}_2)\right]}{D^2+2/\sigma_R^2}\right\}$$

$$\cdot \exp\left\{\frac{-\left(s\frac{\vec{K}_1}{k}-h\frac{\vec{K}_T}{k}\right)^2 - j2\left(s\frac{\vec{K}_1}{k}-h\frac{\vec{K}_T}{k}\right)\frac{D^2}{4}(\vec{K}_T-\vec{K}_1+\vec{K}_2) + \frac{D^4}{16}(\vec{K}_T-\vec{K}_1+\vec{K}_2)^2}{D^2+2/\sigma_R^2}\right\}.$$

Thus, the double integration over $\vec{\rho}_4$ is given by

$$I(\vec{\rho}_4) = c\exp\left\{-\frac{D^2}{8}(K_T-\vec{K}_1+\vec{K}_2)^2\right\}\exp\left\{-j\left[\frac{K_T^2}{2k}h - b + s\frac{K_1^2}{2k}\right]\right\}$$

$$\cdot \exp\left\{\frac{-\left(s\frac{\vec{K}_1}{k}-h\frac{\vec{K}_T}{k}\right)^2 - j2\left(\frac{s\vec{K}_1}{k}-h\frac{\vec{K}_T}{k}\right)\frac{D^2}{4}(\vec{K}_T-\vec{K}_1+\vec{K}_2) + \frac{D^4}{16}(\vec{K}_T-\vec{K}_1+\vec{K}_2)^2}{D^2+2/\sigma_R^2}\right\}$$

$$\cdot \frac{\pi}{\frac{D^2k^2}{4f^2}-\frac{D^4k^2\sigma_R^2}{4f^2D^2\sigma_R^2+8f^2}}$$

$$\cdot \exp\left\{\frac{\left[\frac{kD^2}{4f}(\vec{K}_T-\vec{K}_1+\vec{K}_2)+\frac{\frac{D^2k}{2f}\left[j\left(s\frac{\vec{K}_1}{k}-h\frac{\vec{K}_T}{k}\right)-\frac{D^2}{4}(\vec{K}_T-\vec{K}_1+\vec{K}_2)\right]}{D^2+2/\sigma_R^2}\right]^2}{\frac{D^2k^2}{f^2}-\frac{D^4k^2\sigma_R^2}{f^2(D^2\sigma_R^2+2)}}\right\}.$$

The equation may be written in the following form, and for simplicity, a group of similar terms are shown.

Real exponents

$$\exp\left\{-\frac{D^2}{8}(\vec{K}_T-\vec{K}_1+\vec{K}_2)^2\right\}\exp\left\{\frac{-\left(s\frac{\vec{K}_1}{k}-h\frac{\vec{K}_T}{k}\right)^2+\frac{D^4}{16}(\vec{K}_T-\vec{K}_1+\vec{K}_2)^2}{D^2+\frac{2}{\sigma_R^2}}\right\}\cdot$$

$$\exp\left\{\frac{\frac{k^2D^4}{16}(\vec{K}_T-\vec{K}_1+\vec{K}_2)^2-\frac{D^6k^2}{16}\frac{(\vec{K}_T-\vec{K}_1+\vec{K}_2)^2}{(D^2+2/\sigma_R^2)}-\frac{\left[\frac{D^4k^2}{4}\left(s\frac{\vec{K}_1}{k}-h\frac{\vec{K}_T}{k}\right)^2\right]-\left[\frac{D^8k^2}{64}(\vec{K}_T-\vec{K}_1+\vec{K}_2)^2\right]}{\left[D^2+\frac{2}{\sigma_R^2}\right]^2}}{D^2k^2-\frac{D^4k^2\sigma_R^2}{D^2\sigma_R^2+2}}\right\}$$

Complex components

$$\exp\left\{-j\left[\frac{K_T^2}{2k}h-b+s\frac{K_1^2}{2k}\right]\right\}\exp\left\{-j\frac{\frac{D^2}{2}\left(s\frac{\vec{K}_1}{k}-h\frac{\vec{K}_T}{K}\right)(\vec{K}_T-\vec{K}_1+\vec{K}_2)}{D^2+\frac{2}{\sigma_R^2}}\right\}\cdot$$

$$\exp\left\{\frac{j\frac{D^4k^2}{4}\frac{(\vec{K}_T-\vec{K}_1+\vec{K}_2)}{(D^2+2/\sigma_R^2)}\left(s\frac{\vec{K}_1}{k}-h\frac{\vec{K}_T}{k}\right)-j\frac{D^6k^2}{8}\frac{(\vec{K}_T-\vec{K}_1+\vec{K}_2)}{(D^2+2/\sigma_R^2)^2}\left(s\frac{\vec{K}_1}{k}-h\frac{\vec{K}_T}{k}\right)}{D^2k^2-\frac{D^4k^2\sigma_R^2}{D^2\sigma_R^2+2}}\right\}$$

Constant

$$\frac{1}{j512}\left(\frac{D^2\pi}{\lambda}\right)^2 ka(\vec{K}_T)\,dz\sqrt{\frac{\pi}{\frac{D^2}{4}+\frac{1}{2\sigma_R^2}}\;\frac{\pi}{\frac{D^2k^2}{4}-\frac{D^4k^2\sigma_R^2}{4D^2\sigma_R^2+8}}}$$

By observation, the peak values of this function are located at

$$\vec{K}_T = \vec{K}_1 - \vec{K}_2 \qquad (5.1)$$

and

$$h_o = \frac{\vec{K}_1}{\vec{K}_T}\, s \tag{5.2}$$

as expected from equations (3.3) and (3.4).

Equation (5.2) differs from equation (3.4) in the parameter $\vec{K}_1$ instead of $\vec{K}_2$. This difference is not significant. For any given system, $\vec{K}_1 \cong \vec{K}_2$ within the resolution of the system. Other combinations of terms should provide the precise K_2 relationship inferred for the geometrical analysis. This fact states the importance of the diffraction analysis as a complete study, because the geometrical analysis represents a simplified process.

At the peak position, the whole expression is reduced to

$$i = C_1 \sin\left(h\frac{K_T^2}{2k} - b + s\frac{K_1^2}{2k}\right),$$

where

$$C_1 = \frac{1}{512}\left(\frac{D^2\pi}{\lambda}\right)^2 k\, a(\vec{K}_T)\, dz \sqrt{\frac{\pi}{\frac{D^2}{4}+\frac{1}{\sigma_R^2}}\;\frac{\pi}{\frac{D^2k^2}{4}-\frac{D^4k^2\sigma_R^2}{4D^2\sigma_R^2+8}}}\ .$$

By using an identity for the sine function and handling one of the terms, the expression is reduced to

$$i = C_1 \cos\left(h\frac{K_T^2}{2k} + s\frac{K_1^2}{2k}\right)\sin b\ .$$

For small values of h and s, the cosine of the angle approximates a unity value and thus, the geometrical analysis becomes valid. The term b represents the phase of the perturbation imposed by the slab of turbulence. Also,

$$b = \vec{K}_T \, v_T \, t \ ,$$

where v_T represents the wind velocity.

The group of real exponents represents the amplitude of the signal out of the detector. By approximating its value to one, h is solved for h_o as shown in equation (5.2). By approximating its value to 1/e, h is solved for $h_o + \Delta h$, where Δh represents the spatial resolution of the system. And for very large values of σ_R^2 , the spatial resolution of the system should approximate equation (3.6) of the geometrical analysis.

The spatial filtering techniques offer better ways to understand the velocity structure in the atmosphere through improved measurements. Basic optical spatial filtering instruments are in the technology transfer stage, while more advanced instrumentation requires further developments.

6. REFERENCES

Brown, E. D., and F. F. Hall, Jr., 1978. Advances in atmospheric acoustics. *Rev. Geophys. Space Phys., 16,* 47-101.

Camagni, P., and S. Sandroni (Eds.), 1984, *Optical Remote Sensing at Air Pollution.* Elsevier Press, Amsterdam, Chapter 1.

Churnside, J. H., S. Hanson, and S. F. Clifford, 1990. Wind and turbulence profiles using a two-spatial-filter receiver. *Appl. Opt.,* (in press).

Churnside, J. H., R. J. Lataitis, and R. S. Lawrence, 1988. Localized measurements of refractive turbulence using spatial filtering of scintillations. *Appl. Opt., 27,* 2199-2213.

Clifford, S. F., and J. H. Churnside, 1987. Refractive turbulence profiling using synthetic aperture spatial filtering of scintillation. *Appl. Opt., 26,* 1295-1303.

Clifford, S. F., and R. J. Lataitis, 1987. Spatial and temporal filtering of scintillation in remote sensing. *IEEE Trans. Antennas Propag., AP-35,* 597-604.

Gilman, G. W., H. B. Coxhead, and F. H. Willis, 1946. Reflection of sound signal in the troposphere. *J. Acoust. Soc. Am., 18,* 274.

Goodman, J. W., 1968. *Introduction to Fourier Optics.* McGraw-Hill, Inc., San Francisco, Chapter 4.

Kropfli, R. A., I. Katz, T. G. Konrad, and E. B. Dobson, 1968. Simultaneous radar reflectivity measurements and refractive index spectra in the clear atmosphere. *Radio Sci., 3,* 991.

Lee, R. W., 1974. Remote probing using spatially filtered apertures. *J. Opt. Soc. Am., 64,* No. 10, 1295-1303.

Lee, R. W., and J. C. Harp, 1969. Weak scattering in random media, with applications to remote probing. *Proc. IEEE, 57,* No. 4, 375-406.

Little, C. G., 1969. Acoustic methods for the remote probing of the lower atmosphere. *Proc IEEE, 57,* 571.

McAllister, L. G., J. R. Pollard, A. R. Mahoney, and P. J. R. Shaw, 1969. Acoustic sounding—a new approach to the study of atmospheric structure. *Proc. IEEE, 57,* 579.

Meyer-Arendt, J. R., 1972. *Introduction to Classical and Modern Optics.* Prentice-Hall, Inc., Englewood Cliffs, New Jersey, p. 41.

Ochs, G. R., T. Wang, R. S. Lawrence, and S. F. Clifford, 1976. Refractive-turbulence profiles measured by one dimensional spatial filtering of scintillations. *Appl. Opt., 15,* 2504-2510.

Ochs, G. R., J. J. Wilson, S. Abbott, and R. George, 1988. Crosswind profile model II. NOAA Tech. Memo. ERL WPL-152, NOAA Environmental Research Laboratories, Boulder, CO, 54 pp.

Pierson, W. J., Jr., G. Neumann, and R. W. James, 1955. Practical methods for observing and forecasting ocean waves by means of wave spectra and statistics. U. S. Navy Hydrographic Office, Publ. No. 603, p. 24.

Protheroe, W. M., 1964. The motion and structure of stellar shadowband patterns. *Quart. J. Roy. Meteor. Soc., 90,* 27.

Tatarskii, V. I., 1961. *Wave Propagation in a Turbulent Medium.* Dover Publications, Inc., New York, Chapter 3.

Vernin, J., and F. Roddier, 1973. Experimental determination of two-dimensional spatio-temporal power spectra of stellar light scintillation. *J. Opt. Soc. Am.*, *63*, 270-273.